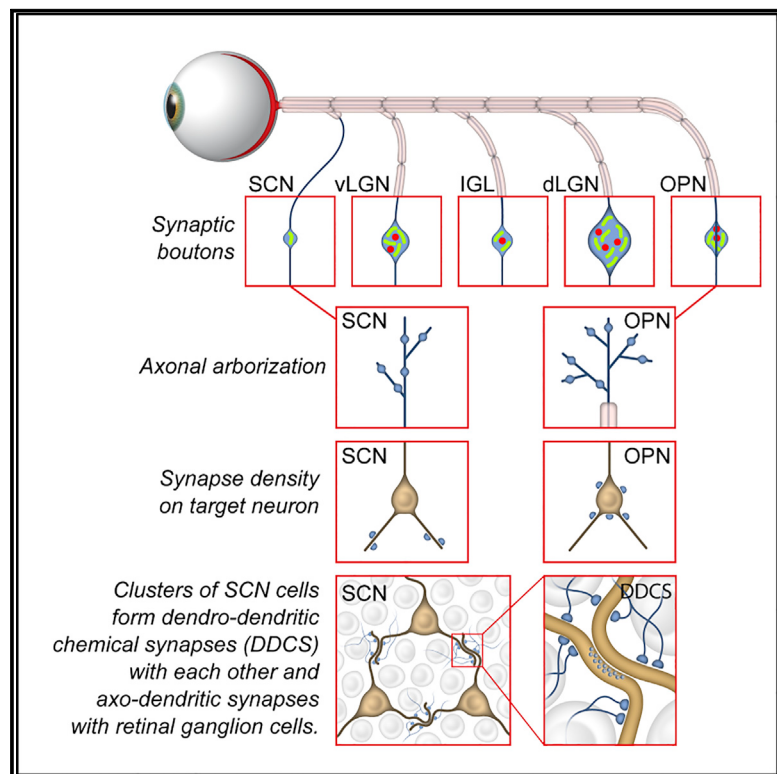


Synaptic Specializations of Melanopsin-Retinal Ganglion Cells in Multiple Brain Regions Revealed by Genetic Label for Light and Electron Microscopy

Graphical Abstract



Authors

Keun-Young Kim, Luis C. Rios, Hiep Le, ..., Megumi Hatori, Mark H. Ellisman, Satchidananda Panda

Correspondence

mellisman@ucsd.edu (M.H.E.), satchin@salk.edu (S.P.)

In Brief

Kim et al. express a genetically encoded electron microscopy (EM) tag in mRGCs of the mouse retina and use serial block-face electron microscopy to analyze the optic nerve and synaptic neuropil in five different brain regions. They find that mRGC synaptic terminals show target-specific specializations corresponding to differences in responses to light.

Highlights

- Membrane-tethered miniSOG for correlated light and electron microscopy *in vivo*
- Melanopsin RGCs show brain region-specific arborization and synaptic structures
- A subset of SCN neurons network through dendrodendritic chemical synapses (DDCS)
- SCN neurons in DDCS network receive a higher melanopsin RGC input



Synaptic Specializations of Melanopsin-Retinal Ganglion Cells in Multiple Brain Regions Revealed by Genetic Label for Light and Electron Microscopy

Keun-Young Kim,^{1,2,7} Luis C. Rios,^{3,7,8} Hiep Le,³ Alex J. Perez,² Sébastien Phan,^{1,2} Eric A. Bushong,^{1,2} Thomas J. Deerinck,^{1,2} Yu Hsin Liu,^{3,4} Maya A. Ellisman,⁵ Varda Lev-Ram,⁶ Suyeon Ju,² Sneha A. Panda,² Sanghee Yoon,² Masatoshi Hirayama,³ Ludovic S. Mure,³ Megumi Hatori,³ Mark H. Ellisman,^{1,2,6,*} and Satchidananda Panda^{3,8,*}

¹Department of Neurosciences, University of California at San Diego School of Medicine, La Jolla, CA, USA

²National Center for Microscopy and Imaging Research, University of California, San Diego, La Jolla, CA, USA

³Salk Institute for Biological Studies, La Jolla, CA, USA

⁴Medical Scientist Training Program, University of California at San Diego School of Medicine, La Jolla, CA, USA

⁵Biological Sciences Graduate Training Program, Division of Biological Sciences, University of California, San Diego, La Jolla, CA, USA

⁶Department of Pharmacology, University of California, San Diego, La Jolla, CA, USA

⁷These authors contributed equally

⁸Lead Contact

*Correspondence: mellisman@ucsd.edu (M.H.E.), satchin@salk.edu (S.P.)

<https://doi.org/10.1016/j.celrep.2019.09.006>

SUMMARY

The form and synaptic fine structure of melanopsin-expressing retinal ganglion cells, also called intrinsically photosensitive retinal ganglion cells (ipRGCs), were determined using a new membrane-targeted version of a genetic probe for correlated light and electron microscopy (CLEM). ipRGCs project to multiple brain regions, and because the method labels the entire neuron, it was possible to analyze nerve terminals in multiple retinorecipient brain regions, including the suprachiasmatic nucleus (SCN), olfactory pretectal nucleus (OPN), and subregions of the lateral geniculate nucleus. Although ipRGCs provide the only direct retinal input to the OPN and SCN, ipRGC terminal arbors and boutons were found to be remarkably different in each target region. A network of dendro-dendritic chemical synapses (DDCSs) was also revealed in the SCN, with ipRGC axon terminals preferentially synapsing on the DDCS-linked cells. The methods developed to enable this analysis should propel other CLEM studies of long-distance brain circuits at high resolution.

INTRODUCTION

Intrinsically photosensitive retinal ganglion cells (ipRGCs) express the photopigment melanopsin (*Opn4*) and are essential for non-image-forming visual processes (Hatori et al., 2008; Hattar et al., 2002). In response to light, ipRGCs fire tonically through the entire duration of light exposure (Berson et al., 2002) and also relay rod/cone-initiated light responses (Wong et al., 2007) via long-range axonal projections to numerous anatomically distinct brain regions regulating different behaviors (Hattar et al., 2006).

In mice, light information travels ~10 mm through ipRGC axons to the suprachiasmatic nucleus (SCN) to facilitate circadian phototransmission and ~15 mm to reach the olfactory pretectal nucleus (OPN) to mediate pupillary constriction in response to light (also known as the pupillary light reflex [PLR]) (Hatori and Panda, 2010; Figure 1A). ipRGC axons also send collaterals to several subregions of the lateral geniculate nucleus (LGN). This diverse pattern of central projections parallels the diversity in photoresponse properties exhibited by these brain regions (e.g., different threshold sensitivities and kinetics). For example, minutes to hours of light exposure are necessary to evoke a saturating phase shift of the SCN clock, whereas a saturating PLR is attained within milliseconds to seconds. How the ipRGC facilitates such temporally and spatially diverse functions remains unknown.

Rod/cone photoreceptors make characteristic synapses with dedicated bipolar and horizontal cells in the retina. These interneurons receive input exclusively from photoreceptors and relay this light information to downstream neurons. It remains unclear whether ipRGCs similarly make relatively homogeneous synaptic contacts with interneurons within target brain regions that receive input exclusively from ipRGCs and subsequently relay this information to other effector neurons. Such region-specific ipRGC target interneurons could help to explain diversities in photoresponses. Alternatively, ipRGCs could make different types of synaptic connections with interneurons within different target brain regions (e.g., synapses of different size or density [or both]), and this could drive region-specific responses to light stimuli. Within each ipRGC recipient brain region, revealing the nature of ipRGC synaptic properties relative to other inputs would provide insight into how light modulates circuit properties. For example, SCN neurons are known to receive synaptic input from at least 5 different types of neurons: ipRGCs in the retina, serotonergic neurons in the raphe nucleus, indirect retinal input from the intergeniculate leaflet (IGL), the paraventricular thalamus, and local input from other SCN neurons (Welsh et al.,



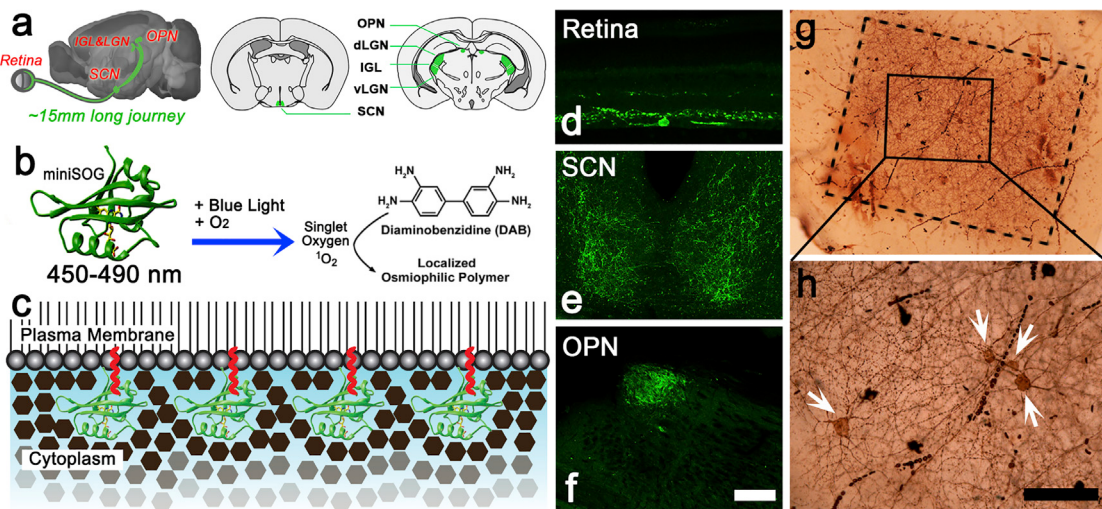


Figure 1. Genetic Labeling of Mouse ipRGCs with Membrane-Targeted MiniSOG

(A) Schematic diagram summarizing the brain regions innervated with ipRGC axons using membrane-targeted miniSOG.
 (B) When excited by blue light, the miniSOG produces singlet oxygen, which quickly oxidizes and polymerizes DAB into a localized osmophilic density.
 (C) MiniSOG-f produces oxidized DAB that can diffuse away and shade the axoplasm with gray.
 (D–H) MiniSOG expression in the vertical retina section (D) and coronal section of the SCN (E) and OPN (F). Note that only illuminated rectangle field (dotted box) shows dark brown DAB reactions in ipRGC somata (arrows) and neurites of the flat-mounted retina, and some red blood cells with endogenous peroxidase showed DAB reactions at low (G) and high (H) magnification under light microscope. Scale bars, 100 μ m. The data in (D)–(H) are from one mouse.

2010). In the absence of quantitative information concerning the relative contribution of each of these inputs (e.g., firing patterns, synaptic strengths, and microcircuitry), it is difficult to assess how SCN circadian neurons integrate and compute these inputs to set the periodicity, phase, amplitude, and synchrony of their oscillations.

Several elegant studies have used automated transmission electron microscopy (Anderson et al., 2011) and serial block-face scanning electron microscopy (SBEM) as a 3D electron microscopy (EM) method to characterize intra-retinal circuitry in the mammalian retina, including that of RGCs (Helmstaedter et al., 2013; Kim et al., 2014). However, there is little data concerning the diversity of synaptic specialization within RGC target regions in the brain. Brain maps that quantify functionally relevant ultrastructural details of synaptic connections are essential to understand the functional anatomy of neuronal circuits. However, the ability to resolve a complete circuit is hindered by the necessity to analyze large volumes of tissue at sufficient resolution, even when using the most advanced 3D electron microscopy methods (Briggman and Bock, 2012). SBEM provides the ultrastructural resolution necessary to visualize and assess single synapses as well as the ability to collect serial images from large volumes of tissue (Denk and Horstmann, 2004). However, the utility of SBEM is currently limited by a number of bottlenecks, including the inability to genetically label specific cell types (Joesch et al., 2016). Genetic labeling of specific cell types would enable mapping of synaptic contacts that are distal from the soma. Several genetically encoded electron microscopy tags (GEM tags) have been developed and tested using *in vitro* systems, but their application to very-long-range projections within *in vivo* brain tissues has been limited (Atasoy et al., 2014). Such genetically encoded electron microscopy tags

include miniSOG (mini-singlet oxygen generator), which is derived from the light oxygen voltage (LOV) domain of *Arabidopsis* phototropin 2 (Figure 1B; Shu et al., 2011). The intrinsic fluorescence of miniSOG, combined with its small size and efficacy as a label in protocols that maintain high-quality ultrastructure for electron microscopy, makes miniSOG an excellent probe for correlated light microscopy and electron microscopy.

For this reason, we designed, refined, and expressed a membrane-tethered version of miniSOG specifically in all ipRGCs in the mouse. Membrane tethering facilitated long-distance tracing of these neurons by labeling the plasma membranes of all axonal processes. After photo-oxidation, we collected SBEM volumes from six tissues and brain regions that contain ipRGC features: optic nerve (ON), SCN, ventral aspect of the LGN (vLGN), IGL, dorsal aspect of the LGN (dLGN), and OPN. Image annotation of SBEM volumes revealed that ipRGCs do not form synapses with interneurons that receive input exclusively from ipRGCs. Instead, ipRGC axons exhibit region-specific branching patterns and synaptic features that are consistent with the functional characteristics of each target brain region. Within the SCN, we found evidence of a small number of SCN neurons that form a network in which they are reciprocally connected with dendrodendritic chemical synapses (DDCSs). ipRGCs preferentially synapse onto SCN neurons interconnected via these DDCSs.

RESULTS

Genetic Labeling of Mouse ipRGCs with Membrane-Targeted MiniSOG Allowed Abundant Labeling of ipRGC Distal Axon Arbors in Brain Regions at Multiscale Levels

We designed an adeno-associated viral vector (AAV) that expresses a C-terminal farnesyl-tagged miniSOG electron

microscopy reporter (Figure 1C) in the presence of Cre recombinase (AAV-EF1 α -DIO-miniSOG-f). The AAV2.2-serotyped EF1 α -DIO-miniSOG-f (1.01×10^{11} genome copy [GC]/mL by qPCR) was intravitreally injected into both eyes of 6-week-old *Opn4*^{Cre/+} mice (Hatori et al., 2008). The specificity of this Cre line and comprehensive expression of this knockin Cre in almost all melanopsin-expressing RGCs have been described before (Brown et al., 2010; Hatori et al., 2008; Mure et al., 2016).

Expression of the miniSOG-f reporter (Figures 1D–1F) in the weeks following vector transduction did not adversely affect circadian rhythm entrainment to the ambient light:dark cycle (Figure S1). Because compromise of ipRGC function would have affected this photoresponse (Kofuji et al., 2016), we conclude that ipRGC function and their connectivity to target brain regions were intact in these ipRGC-labeled mice.

Within the retina, miniSOG expression was restricted to sparse RGCs in the ganglion cell layer. Labeled axons were found in target brain regions, including the SCN and OPN (Figures 1D–1F; Figures S2A–S2I). A portion of the retina was photo-oxidized in the presence of diaminobenzidine (DAB) under blue light irradiation until a light brown precipitate formed in ipRGC cell bodies and neurites (Figures 1G and 1H). The number of ipRGC somata labeled and identified after miniSOG photo-oxidation was $174 \pm 25/\text{mm}^2$ (average \pm SD, n = 6), which is equivalent to the estimated ipRGC density in the mouse retina (Berson et al., 2010).

The membrane-delimited miniSOG enabled specific labeling of all ipRGC axons beyond the retina, confirming that ipRGCs send axon collaterals to the SCN and other brain regions, including the OPN (Fernandez et al., 2016). To resolve the ultrastructure of ipRGCs and their neurites, photo-oxidized tissue sections from the ON and five brain targets (the SCN, dLGN, vLGN, IGL, and OPN) were processed for SBEM as described previously (Deerinck et al., 2010). The IGL receives inputs from ipRGCs and sends afferent projections to the SCN to fine-tune photoentrainment (Brown et al., 2010; Hattar et al., 2006; Mure and Panda, 2012). The dLGN and vLGN are involved in image-forming vision and are known to receive ipRGC input (Brown et al., 2010).

ipRGC Axons Are Myelinated in the ON but Unmyelinated in Their Terminal Fields

By light microscopy (LM), the intrinsic green fluorescence of miniSOG was detectable and distributed in cross-sections of the proximal ON. Photo-oxidation of the ON also revealed miniSOG-positive (miniSOG $^+$) ipRGC axons (Figures 2A–2C). The label could be followed for the entire length of these axons within the imaged volume (Video S1). Although LM-based analysis of ipRGC axons in the retina showed regular clustering of axons as they approached the ON head (Brown et al., 2010), within the ON, ipRGC axons were rarely near one another. ipRGC axon thickness (the diameter of a circle with the same enclosed area as the miniSOG $^+$ axons) within the ON varied between 113 and 1,455 nm (median, 632 nm; n = 44). The distribution of axon diameters reflects the bimodal distribution of ipRGC soma diameters, which is consistent with the notion that axon caliber varies with soma size (Williams and Chalupa, 1983).

Because ipRGC-mediated photo-responses elicit physiological outputs within the SCN and OPN that differ in timescale and, presumably, reliability, it is thought that differential myelination of ipRGC axons may affect the response properties of target neurons. Co-staining for myelin indicated that most miniSOG $^+$ axons within the ON were myelinated (Figure 2D; Figures S2J–S2M). We validated myelination of ipRGC axons in the ON by analyzing thin cross-sections of the ON using transmission electron microscopy (TEM) (Figure S2N). These data also revealed many unmyelinated axons within the ON, none of which were labeled with miniSOG (Figure S2O).

Photo-oxidation of the SCN and OPN revealed miniSOG DAB staining in both of these ipRGC recipient regions, correlating with miniSOG immunoreactivity via LM, and darkly stained axons in SBEM images of these regions (Figures 2E–2L). SBEM imaging reaffirmed that miniSOG $^+$ axons in the OPN were largely myelinated and often contained a heminode, whereas miniSOG $^+$ ipRGC axons in the SCN were primarily unmyelinated (Figures 2G and 2K). Co-staining of myelin using FluoroMyelin in the SCN and OPN of miniSOG-expressing mice showed that the SCN was largely devoid of myelin, whereas the OPN was heavily myelinated (Figures 2H and 2L).

Automatic and Manual Segmentation and Random Sampling of MiniSOG $^+$ Axons in the Brain

MiniSOG protein (Figures 1E and 1F) and brown photo-oxidation products (Figures 2E, 2F, 2I, and 2J) were detectable (prior to osmification) in primary ipRGC target regions of the SCN and OPN. We also collected coronal brain sections containing the IGL, dLGN, and vLGN (Figure 1A; Figure S3). The SBEM 3D image stacks of these 5 brain regions (each at least 10 mm from the retina in the mouse) showed contiguously stained miniSOG $^+$ neurites that could be visually distinguished from other neurites in these brain regions.

Double staining the SCN for ipRGC axons and vasoactive intestinal peptide (VIP) revealed that ipRGC axons densely innervated the core (ventral) aspect of the SCN (Figures 2M and 2N). We photo-oxidized coronal brain sections containing the SCN and chose core regions of the SCN for subsequent SBEM imaging (Figures 2O–2Q). Using IMOD software (Anderson et al., 2003; Kremer et al., 1996), we manually segmented all miniSOG $^+$ axons and processed a 2.5 billion voxel volume ($5,000 \times 5,000 \times 100$) of the SCN to be used as a training set to optimize automatic segmentation. The dense miniSOG labeling of axolemma and axoplasm in ipRGC nerve fibers within the SCN and the lack of myelination in the SCN facilitated automatic segmentation of ipRGC axon segments in the SCN core region. The cascaded hierarchical model (CHM), a 2D supervised pixel classification framework (Seyedhosseini et al., 2013), was employed to generate dataset-wide segmentations of miniSOG $^+$ axons (Perez et al., 2014). The automatic segmentation algorithm in the SCN achieved a precision (fraction of ground truth reported true positive), recall (fraction of ground truth predicted by the algorithm), and F-value of 0.66926, 0.66153, and 0.66537, respectively (Figures 2R–2T). Application of the same algorithm to the rest of the SCN automatically segmented at least a portion of the ipRGC axons within the entire volume (Figures 2U and 2V, green), facilitating rapid assessment of the distribution and

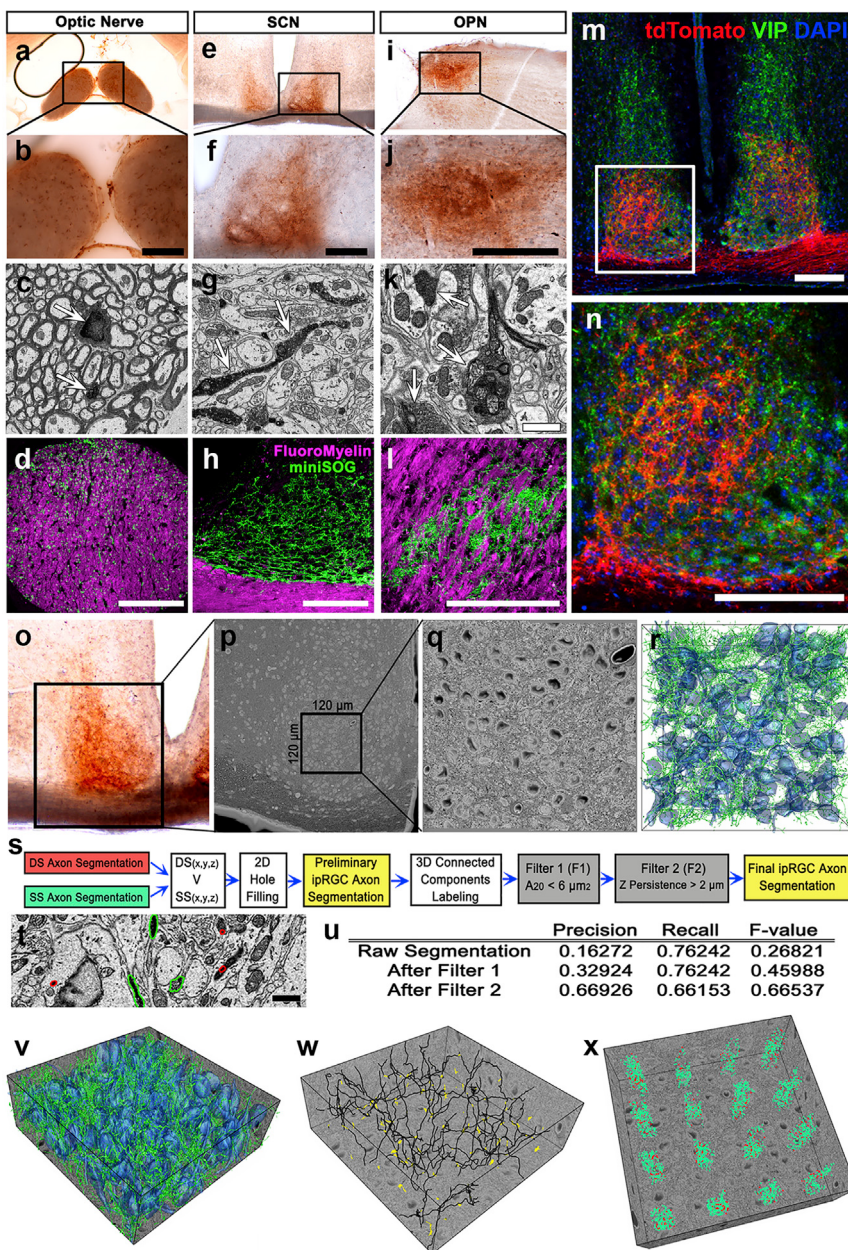


Figure 2. Automatic and Manual Segmentation and Random Sampling of MiniSOG⁺ Axons in Brain Regions

(A–C, E–G, and I–K) Correlated transmitted light and electron microscopy imaging of photo-oxidized ipRGCs axons in the ON (A–C), SCN (E–G), and OPN (I–K). The differential contrast generated between a transfected ipRGC axons (arrows) and non-transfected axons is evident (C, G, and K).

(D, H, and L) Immunolabeling with anti-miniSOG (green) and FluoroMyelin staining (magenta) showed myelinated ipRGC axons in the ON (D) and OPN (L) but are not in the SCN (H).

(M and N) Double-labeling of ipRGC axons (tdTomato, red) and VIP (green) in the coronal section of the SCN showed VIP somas predominantly in the ventral aspect, whereas their processes elongate to the dorsal aspect at low magnification (M) and higher magnification (N).

(O–Q) An LM image following photo-oxidation (O) and a block surface image showing the correlated SCN area (P). The core region of the SCN was used for SBEM. Volume dimension; x, y, and z = 120 μm, 120 μm, and 30 μm (Q).

(R) Automatic segmentation of the miniSOG transfected ipRGC axons (green) and manual segmentation of the SCN neuron (blue) throughout the whole SBEM volume.

(S–U) Automated segmentation strategy for variably stained ipRGC axons. Densely stained (DS) axons demonstrated a consistent dark staining pattern. Sparsely stained (SS) axons exhibited a consistent lighter staining pattern across the volume. After a series of filters (STAR Methods), the final miniSOG-positive axons were retained (S). Segmentation results overlay an image slice from the SBEM volume. Contours outlined in green satisfied filter criteria, whereas contours outlined in red were rejected and removed from the final segmentation (T). Segmentation results over a sub-volume of 5,000 × 5,000 × 100 voxels were compared with ground truth manually segmented from the same sub-volume. Increases in precision and F-value were obtained as a result of the applied filters (U).

(V and W) In addition to automatic segmentation (V), 100 random miniSOG boutons (yellow) and their axonal arbors (black) were manually traced (W).

(X) Random sub-volume columns for unbiased bouton density measurement.

Scale bars, 100 μm (B, D, F, H, J, and L–N) and 1 μm (C, G, K, and T). The images in (D), (H), and (L)–(N) are representative of 3 mice; all other data are from one mouse.

See also Figures S2 and S3.

density of miniSOG⁺ neurites within the volume. The portion of miniSOG⁺ neurites that could not be accurately autosegmented often had nearby darkly stained intracellular organelles (Figure 2T). Automatic segmentation confirmed that the entire SCN tissue block was innervated by ipRGC axons and that miniSOG⁺ axons were photo-oxidized throughout the volume (Video S2).

In the OPN, IGL, dLGN, and vLGN, darkly stained, myelinated, non-ipRGC axons could be visually distinguished from miniSOG⁺ axons. However, the automatic segmentation algorithm could

not efficiently distinguish between thin myelinated non-ipRGC axons and miniSOG⁺ ipRGC axons. This limitation prompted us to devise an alternative random sampling approach that could be applied to all brain regions. The xy plane from volumes of all brain regions was overlaid with an 11 × 11 equally spaced grid. Selecting the miniSOG⁺ features closest to the intersection of grid lines along the z axis offered an unbiased sampling of 100 ipRGC neurites in all brain regions (Figure 2W; Figure S3). Similarly, a random sampling from sub-volume columns offered an unbiased sampling of volume-based measurements of

labeled ipRGC features as well as unlabeled ultrastructural features in the SCN (Figure 2X) and other ipRGC recipient brain regions.

ipRGCs Form Distinct Types of Synaptic Boutons in Different Target Brain Regions

MiniSOG⁺ ipRGC axons had occasional swellings that resembled synaptic boutons (Figure S3). Double-tilt intermediate high-voltage electron tomography (ET) of 250-nm sections of the SCN and OPN confirmed that these synaptic swellings contained synaptic vesicles, mitochondria, and, occasionally, dendritic spine-like processes (Figures 3A–3D; Video S3). These boutons were also accompanied by prominent post-synaptic densities in apposed dendrites, consistent with excitatory synapses. Therefore, for subsequent analyses, we operationally defined an axonal swelling with synaptic vesicles and a postsynaptic density as a synaptic bouton.

Randomly sampled synaptic boutons along miniSOG⁺ ipRGC axons in the SCN and OPN showed characteristic features with respect to mitochondrial content (green) and spine intrusions (or spinules, red) (Figures 3B and 3D–3F). We segmented 100 or more randomly sampled miniSOG⁺ ipRGC boutons from the dLGN, IGL, and vLGN. ipRGC boutons showed region-specific differences in features that likely contribute to synaptic strength: size, spinules, and mitochondrial content. ipRGC bouton volume showed nearly 6-fold variations between target brain regions, with the largest boutons in the dLGN and the smallest boutons in the SCN (Figures 3G–3I; Table 1). More than 50% of ipRGC boutons contained at least one synaptic spinule in the dLGN, vLGN, OPN, and IGL, but such boutons were less frequent in the SCN (20% ± 4.0%, n = 100) (Figure 3K). Among boutons with synaptic spinules, the average number of spinules per bouton was 2.5 times more in the dLGN than the lowest number found in the SCN (Figure 3L). The number of mitochondria per bouton also varied by over 4-fold, with the highest levels in the dLGN and lowest levels in the SCN (Figure 3M; Table 1).

We then determined whether differences in ipRGC bouton volumes between the OPN and SCN depended on the brain region into which they projected or were simply unique to the ipRGC boutons. Randomly picked non-ipRGC boutons, which come from other regions of the brain and from within the nucleus, were of similar size as ipRGC boutons in the OPN but larger than ipRGC boutons in the SCN (Figure 3N; Table 2; Table S1).

Each synaptic bouton can make synaptic contact with one or more dendrites. Although ipRGC boutons in the OPN were more than 2 times larger than in the SCN, the number of dendrites with which each bouton made synaptic contacts was slightly less in the OPN than in the SCN (Figure 3O). Therefore, in the OPN, boutons with larger volumes and more mitochondria were not associated with a greater number of synaptic partners. Rather, in the OPN, a larger fraction of bouton volume was available to each synaptic dendrite (0.65 ± 0.05 μm³) than in the SCN (0.27 ± 0.02 μm³) (Figure 3P).

The Density of ipRGC Boutons Varies between Target Brain Regions

To assess the overall density of ipRGC boutons, the tissue was subdivided into 81 cuboid columns using a 9 × 9 grid. All ipRGC

boutons in 16 (~20%) evenly dispersed columns were manually verified. The number of ipRGC boutons per 1,000 μm³ of tissue surveyed was 8–9.5 in the vLGN, OPN, IGL, and SCN and nearly 4-fold less in the dLGN (Figure 3Q; Table 1).

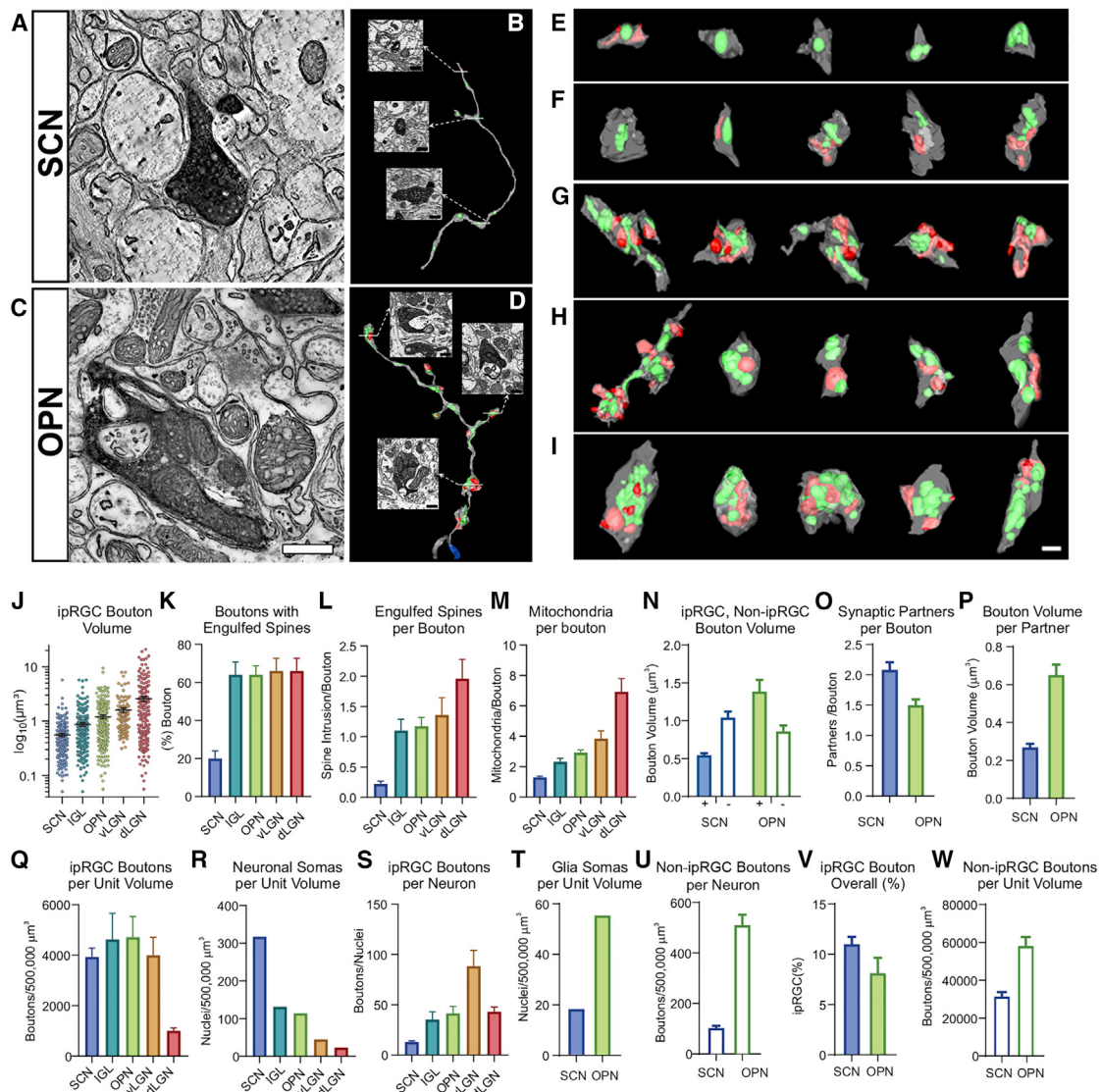
We manually segmented all nuclei within the entire volume in the dLGN, vLGN, OPN, IGL, and SCN. Each soma was then determined to be a neuron or a glial cell by assessing its morphology. The number of neuronal somata per unit volume (500,000 μm³) varied over an order of magnitude, with the lowest number in the dLGN (23.3) and the highest in the SCN (317.0) (Figure 3R; Table 1). The number of ipRGC boutons per neuron was estimated to be greatest in the vLGN (88.49 ± 11.78) and lowest in the SCN (13.01 ± 1.15) (Figure 3S; Table 1). Glial cell concentration was higher in the OPN (n = 55.7/500,000 μm³) compared with the SCN (n = 18.6/500,000 μm³) (Figure 3T).

To assess the relative abundance of ipRGC boutons, non-ipRGC boutons in the OPN and SCN were manually verified in the same columns in which we sampled ipRGC boutons. The concentration of non-ipRGC boutons was much greater in the OPN (116.83 ± 8.92/1000 μm³; n = 3,499 boutons; surveyed volume = 29,949 μm³) than in the SCN (63.55 ± 3.87; n = 2,850 boutons; surveyed volume = 36,438 μm³). The overall proportion of ipRGC boutons in the OPN (8.19% ± 1.03%) tended to be less than in the SCN (11.05% ± 0.69%), although this was not significant (p = 0.11) (Figure 3V). Reflecting the higher concentration of neuropil, non-ipRGC boutons per neuron were much greater in the OPN (561.90 ± 26.51) compared with the SCN (122.37 ± 7.40) (Figure 3W; Table 2). In general, the properties of ipRGC boutons and their proportional input to recipient neurons varied between target brain regions.

Distinct Patterns of ipRGC Axon Arborization in the OPN and SCN

Axons connected to the 100 grid-selected ipRGC boutons were extended and fully traced within the SCN and OPN volumes. In some instances, such randomly selected boutons were of the same axonal arbor. This resulted in complete reconstruction of 61 distinct axonal arbors in the OPN and 88 axonal arbors in the SCN. In the OPN, the 61 axonal arbors totaled 12,115 μm in length and contained 1,229 synaptic boutons and 690 non-synaptic swellings. Based on the bouton density estimates above, this sampling represented 24.2% ± 4.2% of all ipRGC boutons in the imaged volume. In the SCN, the 88 axonal arbors totaled 6,522 μm in length and contained 540 synaptic boutons and 192 non-synaptic swellings. We estimate that this represented 17.8% ± 1.6% of all ipRGC boutons in the volume (Figures 4A and 4B). Although SCN and OPN volumes were of comparable sizes, randomly selected ipRGC axonal arbors were less branched in the SCN than in the OPN (Figures 4C and 4D; Figures S4 and S5).

We measured axon diameters at regions distal from boutons or a swelling, revealing that axons in the OPN had a larger basal diameter than in the SCN (Figure 4E). Furthermore, in the OPN, 10% of ipRGC axons that made synapses in the sample contained one or more patches of myelin, and there were numerous myelinated passing fibers. In contrast, ipRGC axons in the SCN were unmyelinated. The axonal arbors in the OPN

**Figure 3. ipRGCs Make Distinct Synaptic Boutons in Target Brain Regions**

(A and C) Representative cross-sections of miniSOG⁺ ipRGC boutons in the SCN (A) and OPN (C) captured with double-tilt ET.

(B and D) In the SCN (B) and in OPN (D) 3D model of an ipRGC axon showing mitochondria (green), engulfed dendritic spines (red), axons (white), and myelin (blue).

(E–I) Representative 3D models of randomly sampled ipRGC boutons in the SCN (E), OPN (F), IGL (G), vLGN (H), and dLGN (I).

(J) Randomly sampled and manually segmented ipRGC bouton volumes in target regions shown in log₁₀ scale; all regions significantly differed from each other ($p < 0.005$).

(K) The proportion of boutons with at least one engulfed spine.

(L) Mean number of engulfed spines per bouton in target regions.

(M) Mean number of mitochondria per bouton.

(N) Randomly sampled non-ipRGC boutons (miniSOG⁻) versus ipRGC boutons (miniSOG⁺) in the SCN and OPN.

(O) Mean number of distinct synaptic partners on each bouton.

(P) Bouton volume per synaptic partner.

(Q) ipRGC bouton estimate per SBEM (500,000 μm³).

(R) Number of neuronal somata per SBEM (500,000 μm³).

(S) ipRGC bouton-to-neuron ratio.

(T) Glial somata per SBEM (500,000 μm³).

(U) Non-ipRGC boutons per SBEM (500,000 μm³).

(V) ipRGC boutons overall (percent).

(W) Non-ipRGC boutons per neuron.

All statistical tests and significant differences between groups are shown in Table 1 and 2 and Table S1. All data are from tissues collected from one mouse. Scale bars, 0.5 μm (A–D) and 1 μm (E–I).

Also see Figure S3.

Table 1. Quantification of Neuronal and Synaptic Features Measured in Different Brain Regions

Features	SCN	OPN	IGL	vLGN	dLGN
Volume of ipRGC boutons	0.55 $\mu\text{m}^3 \pm 0.04$, n = 203 ^a	1.18 $\mu\text{m}^3 \pm 0.09$, n = 189 ^{a,b}	0.99 $\mu\text{m}^3 \pm 0.04$, n = 130 ^{b,c}	1.51 $\mu\text{m}^3 \pm 0.17$; n = 100 ^c	3.24 $\mu\text{m}^3 \pm 0.53$, n = 124 ^d
Percentage of ipRGC boutons with at least one spine intrusion (spinule)	20% $\pm 4.0\%$, n = 100 ^a	64% $\pm 4.8\%$, n = 100 ^b	64% $\pm 4.8\%$, n = 50 ^b	66% $\pm 6.8\%$, n = 50 ^b	66% $\pm 6.8\%$, n = 50 ^b
Spinules/bouton among spinule-positive ipRGC boutons	1.10 ± 0.07 , n = 20 ^a	1.83 ± 0.19 , n = 64 ^b	1.72 ± 0.23 , n = 32 ^b	2.06 ± 0.38 , n = 33 ^{b,c}	2.97 ± 0.37 , n = 33 ^c
Mitochondria/ipRGC bouton	1.29 ± 0.08 , n = 100 ^a	2.91 ± 0.19 , n = 100 ^{a,b}	2.32 ± 0.24 , n = 50 ^{b,c}	3.84 ± 0.54 , n = 50 ^{c,d}	6.93 ± 0.85 , n = 50 ^{d,e}
Number of ipRGC boutons/1,000 μm^3	7.87 ± 0.69 , n = 353 boutons, total surveyed volume = 44,846 μm^3 ^a	9.44 ± 1.63 , n = 565 boutons, total surveyed volume = 59,899 μm^3 ^a	9.26 ± 1.78 , n = 198 boutons, total surveyed volume = 21,381 μm^3 ^a	8.00 ± 1.06 , n = 283 boutons, total surveyed volume = 35,381 μm^3 ^a	2.01 ± 0.21 , n = 149 boutons, total surveyed volume = 74,240 μm^3 ^b
Number of neuronal somata/500,000 μm^3	317.0	114.1	131.7	45.2	23.3
Number of ipRGC boutons/neuron	13.01 ± 1.15 ^a	41.40 ± 7.16 ^{a,b}	35.21 ± 6.78 ^b	88.49 ± 11.78 ^c	43.10 ± 4.54 ^b

ipRGC boutons exhibit region-specific specialization in five different retinofugal brain nuclei examined. A summary of statistical analyses is shown in Table S1.

^aipRGC boutons exhibit region-specific specialization in five different retinofugal brain nuclei examined.

^bFeatures of ipRGC axonal arbors and synapses in the SCN and OPN.

^cQuantitative assessment of ipRGC boutons in proximal and distal SCN dendrites in relation to the presence of DDCSs.

^dGroups that are not statistically different share the same letter.

^ens, not significant.

were almost twice as large as those in the SCN. The larger axonal arbor was due to more than 2-fold more branchpoints per axon in the OPN than in the SCN (Figures 4F and 4G; Table 2). Furthermore, the difference in axon size between the SCN and OPN was partially explained by a longer distance between branchpoints in the OPN compared with the SCN (Figure 4H). The terminal branch length, defined as the distance from the end of a terminating node to a branchpoint, was similar in the two brain regions (Figure 4I).

Although synaptic boutons in the OPN were larger, both OPN and SCN ipRGC axons had non-synaptic swellings of similar size (Figure 4J). These non-synaptic swellings contained a single mitochondrion and were often engulfed either partially or entirely by a glial process. ipRGC axons in the OPN had more non-synaptic swellings per 100 μm axon length (5.99 ± 0.55) than in the SCN (2.99 ± 0.24) (Figure 4K). However, the number of synaptic boutons per 100 μm axon length was not significantly different between the OPN and SCN (Figure 4L; Table 2). Considering that the number of boutons per length was comparable and that there were slightly more synaptic partners per bouton in the SCN than in the OPN, the higher frequency of non-synaptic mitochondria implies a greater number of mitochondria dedicated to each synaptic partner in the OPN. Taken together with bouton and mitochondrial frequency, the available pool of mitochondria per 100 μm axon length was more than 2-fold higher in the OPN than in the SCN.

ipRGCs Prefer Distal Dendrites in the SCN but Proximal Dendrites and Somata in the OPN

To unambiguously define proximal and distal dendrites, we mapped synaptic density as a function of distance from the soma in the SCN. We first segmented all somata with a nucleus within the analyzed volume (n = 286) (Figures 2R and 2V, blue) and skeletonized all dendrites (n = 398, total length = 14,396 μm) emanating from those somata. All synapses, both ipRGC and non-ipRGC, on the 15 longest SCN dendrites (>90 μm) were mapped as a function of dendritic distance from the soma in 10- μm bins. Non-ipRGC synapses were uniformly distributed along the dendrite, whereas the abundance of ipRGC synapses along SCN dendrites fit a sigmoid curve ($R^2 = 0.78$) with an inflection point near 75 μm . Therefore, the first 75 μm of an SCN dendrite were considered proximal and the region beyond 75 μm distal. The function predicts 1 ipRGC input per 75 μm proximal dendritic length, rising to 5 ipRGC inputs per 75 μm in the most distal region (Figure 5A). ipRGC boutons as a fraction of all boutons also showed a similar sigmoid curve ($R^2 = 0.86$, linear fit $R^2 = 0.73$) that began with ~2% ipRGC synapses in proximal regions and ~20% ipRGC synapses in the most distal regions (Figure 5B). The previous column-based sampling measurement of 11% (Figures 3Q and 3U) represented a volumetrically weighted average of both proximal and distal ipRGC synapse proportions throughout the tissue.

To test whether this model, which was based on a select set of 15 dendrites, applied to the rest of the SCN, we randomly

Table 2. Features of ipRGC Axonal Arbors and Synapses in the SCN and OPN

Features	OPN	SCN
Number of non-ipRGC boutons/500,000 μm^3	$58,432 \pm 4,461$, n = 3,499 boutons, surveyed volume = 29,949 μm^3 ^a	$31,775 \pm 1,934$, n = 2,850 boutons, surveyed volume = 36,438 μm^3 ^b
Volume of non-ipRGC boutons	$0.86 \mu\text{m}^3 \pm 0.09$, n = 100, ns	$1.05 \mu\text{m}^3 \pm 0.09$, n = 100, ns
Number of glia/500,000 μm^3	55.7	18.6
Number of synapses/ipRGC bouton	1.51 ± 0.09 , n = 67 ^a	2.09 ± 0.13 , n = 77 ^b
ipRGC bouton volume/synaptic partner	$0.65 \mu\text{m}^3 \pm 0.05$ ^a	$0.27 \mu\text{m}^3 \pm 0.02$ ^b
Percentage of all boutons that are ipRGC positive	$8.19\% \pm 1.03\%$, ns	$11.05\% \pm 0.69\%$, ns
Non-ipRGC boutons/neuron	561.90 ± 26.51 ^a	122.37 ± 7.40 ^b
ipRGC axon diameter	$211 \text{ nm} \pm 1.90$, n = 20 axons, n = 275 measurements ^a	$182 \text{ nm} \pm 1.5$, n = 20 axons, n = 345 measurements ^b
Size of the ipRGC axon arbor contained in the imaged volume	$184.31 \mu\text{m} \pm 34.77$ ^a	$91.83 \mu\text{m} \pm 5.94$ ^b
Branchpoints/ipRGC axon in the imaged volume	4.65 ± 1.08 ^a	1.99 ± 0.29 ^b
Distance between ipRGC axon branchpoints	$15.9 \mu\text{m} \pm 1.7$, n = 84 ^a	$10.2 \mu\text{m} \pm 1.6$, n = 41 ^b
ipRGC terminal branch length	$9.6 \mu\text{m} \pm 1.3$, n = 62, ns	$8.3 \mu\text{m} \pm 1.1$, n = 60, ns
Volume of non-synaptic swellings on axons	$0.28 \mu\text{m}^3 \pm 0.02$, n = 91, ns	$0.27 \mu\text{m}^3 \pm 0.03$, n = 66, ns
Non-synaptic swellings per 100 μm axon length	5.99 ± 0.55 ^a	2.99 ± 0.24 ^b
Number of synaptic boutons per 100 μm axon length	9.76 ± 0.63 , ns	8.86 ± 0.59 , ns
Number of ipRGC synapses on somata	6.18 ± 1.60 , n = 17, ns	1.68 ± 1.25 , n = 19, ns
ipRGC boutons on proximal dendrites	8.09 ± 1.42 , n = 18 neurons ^a	1.70 ± 0.29 , n = 77 neurons ^b
ipRGCs per 1,000 μm^2 of proximal dendrite surface area	16.18 ± 2.01 , n = 18 cells ^a	6.20 ± 1.08 , n = 17 cells ^b
ipRGC synapses on somata	$19.15\% \pm 2.52\%$, n = 18 ^a	$6.63\% \pm 1.77\%$, n = 40 ^b
ipRGC synapses on proximal dendrites	$17.26\% \pm 3.46\%$, n = 18 ^a	$8.71\% \pm 1.31\%$, n = 23 ^b

Groups that are not statistically different share the same letter. ns, not significant. A summary of statistical analyses is shown in Table S1.^aipRGC boutons exhibit region-specific specialization in five different retinofugal brain nuclei examined.

^bFeatures of ipRGC axonal arbors and synapses in the SCN and OPN.

sampled 100 SCN dendrites and traced these in their entirety. The random cohort of 100 dendrites had 24 dendrites that mapped back to somata; hence, ~24% of dendrites within the volume were proximal dendrites. We resampled the grid to obtain an unbiased cohort of 100 distal-only dendrites and marked all ipRGC synapses on these dendrites. The mean synaptic density in these distal SCN dendrites was close to the predicted value of 5 ipRGC synapses per 75 μm (4.88 ± 0.49 , n = 100). Upon marking both ipRGC and non-ipRGC synapses on randomly selected SCN distal dendrites, we found that an average of $19.18\% \pm 1.97\%$ (n = 11) synapses were ipRGC synapses, which was close to the previous estimate.

Next we asked whether ipRGCs preferentially innervated the somata, proximal dendrites, or distal dendrites in both the SCN and OPN. The lower density of nuclei in the IGL, dLGN, and vLGN precluded this analysis in those volumes. We mapped ipRGC boutons onto the somata and proximal 75 μm of all dendrites for 18 OPN neurons and 77 SCN neurons in the central area of each SBEM volume (a subset is shown in Figures 5C and 5D). Only one of 18 OPN neurons (5.56%) did not have any ipRGC synapses on the somata, whereas 52.5% of SCN somata lacked an ipRGC synapse (Figure 5E). Among somata with 1 ipRGC synapse or more, OPN somata received a higher number of ipRGC synapses than SCN somata (Figure 5F). ipRGC boutons were more abundant in proximal regions of OPN neu-

rons compared with the proximal regions of SCN neurons (Figure 5G). However, there were 13 SCN neurons that received a disproportionately higher number of ipRGC boutons in the proximal dendrites. Many of these dendrites were found to be part of a network that is preferred by ipRGCs (see next section).

To account for potential differences in dendritic thickness, we manually segmented all 18 OPN neurons and the most central 23 neurons in the SCN to the full extent captured in the volume (Videos S4 and S5) marking both ipRGC and non-ipRGC synaptic boutons. Among neurons with 1 ipRGC bouton or more, proximal ipRGC boutons per 1,000 μm^2 surface area were 2.6 times higher in the OPN than in the SCN (Figure 5H). In the OPN, the proportion of ipRGC to non-ipRGC synapses was highest on the soma, intermediate on the proximal dendrite, and lowest in the tissue overall, which would indicate the lowest concentration on the distal dendrite. In the SCN, we observed the opposite trend, with the lowest proportion on the soma, intermediate on the proximal dendrite, and highest in the tissue overall (Figure 5I), which would indicate the highest concentration on the distal dendrites (estimated to be $19.18\% \pm 1.97\%$).

Each ipRGC Axon Arbor Formed Synapses with Multiple Recipient Neurons

To assess the neuronal preference of ipRGC input in the SCN, we marked all synaptic boutons in 36 evenly distributed and

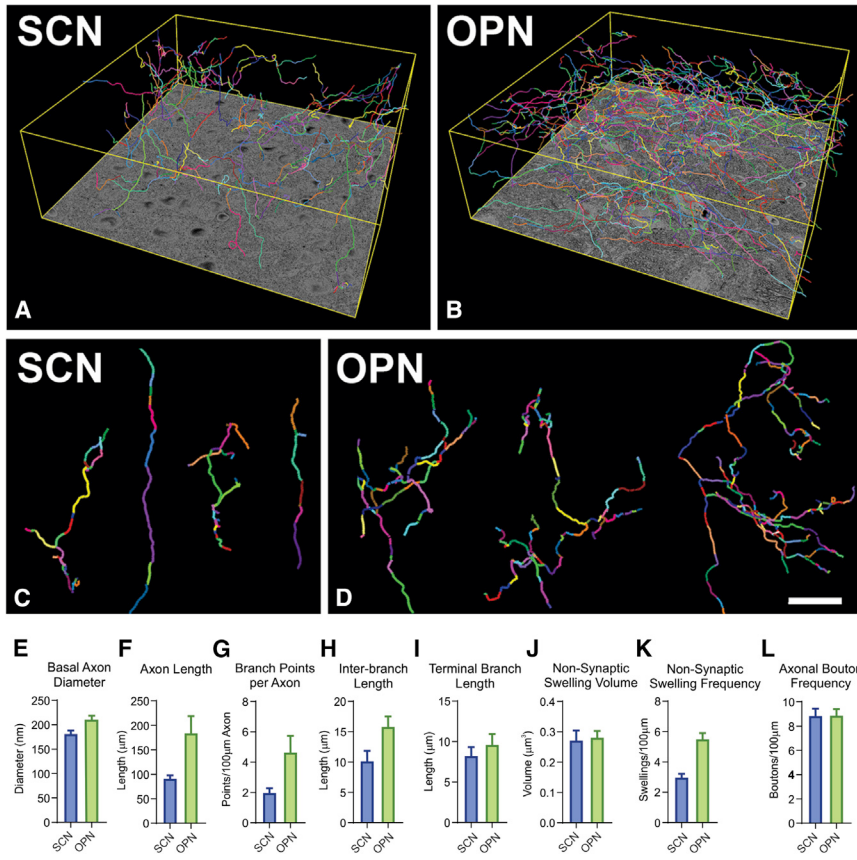


Figure 4. Randomly Sampled ipRGC Axons in the SCN and OPN

(A and B) 3D view of 88 ipRGC axonal arbors in the SCN (A) and 61 axonal arbors in the OPN (B).

(C and D) Representative individual ipRGC axons in the SCN (C) and OPN (D).

(E) Basal axon diameter at points distal from a bouton or swelling; $p = 0.003$.

(F) Axon length, $p = 0.011$.

(G) Branchpoints per axon, $p = 0.007$.

(H) Inter-branch length, $p = 0.033$.

(I) Terminal branch length, not significant, $p = 0.43$.

(J) Non-synaptic swelling volume, not significant, $p = 0.155$.

(K) Non-synaptic swelling frequency, $p < 0.0001$.

(L) Bouton frequency within the axon, not significant, $p = 0.96$.

All data are from tissues collected from one mouse. Scale bar, 20 μm .

See also Figures S4 and S5.

randomly selected ipRGC axonal arbors. These 36 axons totaled 3,072 μm in length and contained 256 synaptic boutons. For simplicity, we will refer to this ensemble of ipRGC synaptic contacts as the projectome. Based on the previously estimated bouton density ($3,028 \pm 268$ total boutons in the imaged volume), 256 projectome boutons represented $8.5\% \pm 0.8\%$ of all ipRGC boutons in the volume. For each bouton, postsynaptic dendrites were traced back in their entirety. We found that many ipRGC boutons formed synapses with more than one postsynaptic partner, with some boutons forming multiple synapses with the same dendrite. Thus, the 256 boutons on 36 axons formed 502 contact sites with 298 distinct cells and dendrites. Because 36 ipRGC axon arbors formed synapses with 298 distinct dendrites and cell bodies, it is safe to conclude that each ipRGC forms synapses with more than one SCN neuron.

Because each postsynaptic dendrite was manually traced back to the cell body, and the presynaptic ipRGC axons were already annotated, we could also determine whether postsynaptic dendrites or neurons receive synaptic input from more than one ipRGC axon. With only 8.5% of axons sampled, 87 of 298 targets (29.2%) were synapsed upon by more than one sampled axon, demonstrating that each SCN neuron receives input from more than one of the ipRGC's terminal axons. Because the SCN receives a nearly equal proportion of retinal input from the ipsi- and contralateral retina, it is safe to assume that nearly half of the randomly sampled SCN axonal arbors were ipsi- and contralateral and represented distinct ipRGCs. In summary, each ipRGC axon made

synaptic contact with multiple SCN neurons and each SCN neuron received input from multiple ipRGC axons. This observation prompted us to examine clusters of SCN dendrites more closely. We discovered a network of SCN neurons that were robustly interconnected via DDCSs. DDCSs are classical synapses between the dendrites of two different neurons, lacking a postsynaptic density (Shepherd, 2009). In several brain regions, DDCSs occur with high fidelity between certain types of GABAergic interneurons (Shepherd, 2009). GABAergic interneurons are abundant in the SCN, particularly in the SCN core (Moore et al., 2002). Sparse DDCSs have been reported for SCN dendrites (Güldner and Wolff, 1974). These DDCSs are asymmetric, lack a postsynaptic density, and contain small irregularly shaped presynaptic vesicles that average 28.4 nm in diameter. These morphological features are consistent with inhibitory synapses (Palay and Palade, 1955). An electron microscopy study of GABAergic SCN neurons indicated that these asymmetric synapses may be present on some dendrites (Castel and Morris, 2000).

Because the number of DDCSs is relatively low in the rodent SCN compared with classical axo-dendritic synapses (Güldner, 1976), we exhaustively surveyed 737 dendrites from three partially overlapping dendrite cohorts in the SCN for the presence of DDCSs. These cohorts were proximal dendrites ($n = 398$), randomly selected dendrites ($n = 100$), and all dendrites that were synapsed upon by 38 randomly selected ipRGC axonal arbors (projectome dendrites, $n = 298$) (Figure S7). Based on the overlap between these three cohorts, we estimated that these 737 dendrites represented close to 50% of all dendrites in the

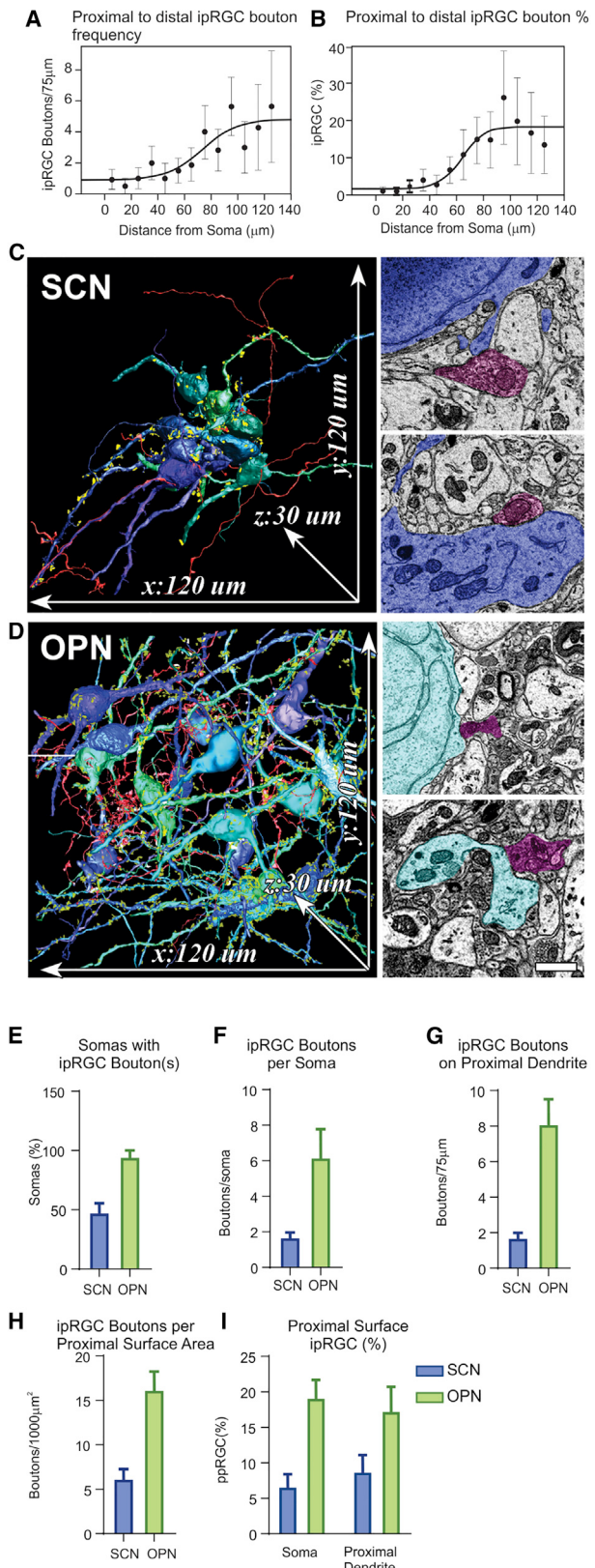


Figure 5. ipRGC Synapses on Segmented Neurons in the SCN and OPN

(A) ipRGC synaptic density on segments of dendrites ranging from 0–140 μm from the soma in the SCN.

(B) Proportion (percent) of ipRGCs to total synaptic boutons on segments of dendrites ranging from 0–140 μm from the soma in the SCN.

(C and D) 3D view of the 10 most central neurons in the SCN (C) and the 16 most central neurons in the OPN (D) with ipRGC axons (red) and all non-ipRGC synapses (yellow) and 2D images of ipRGC boutons (magenta) and neurons (blue) in the SCN and turquoise in the OPN.

(E) Proportion of neuronal somata with at least 1 ipRGC synapse; $p < 0.0001$.

(F) ipRGC synaptic frequency on the first 75 μm of dendrite; $p < 0.0001$.

(G) ipRGC boutons per proximal surface area; $p = 0.0002$.

(H) ipRGC boutons per soma among somata with at least 1 ipRGC synapse; $p = 0.015$.

(I) ipRGC bouton proportion (percent) on a soma (SCN versus OPN, $p = 0.0002$) and proximal dendrite (SCN versus OPN, $p = 0.043$). There was no significant difference between the soma and proximal dendrite within a region.

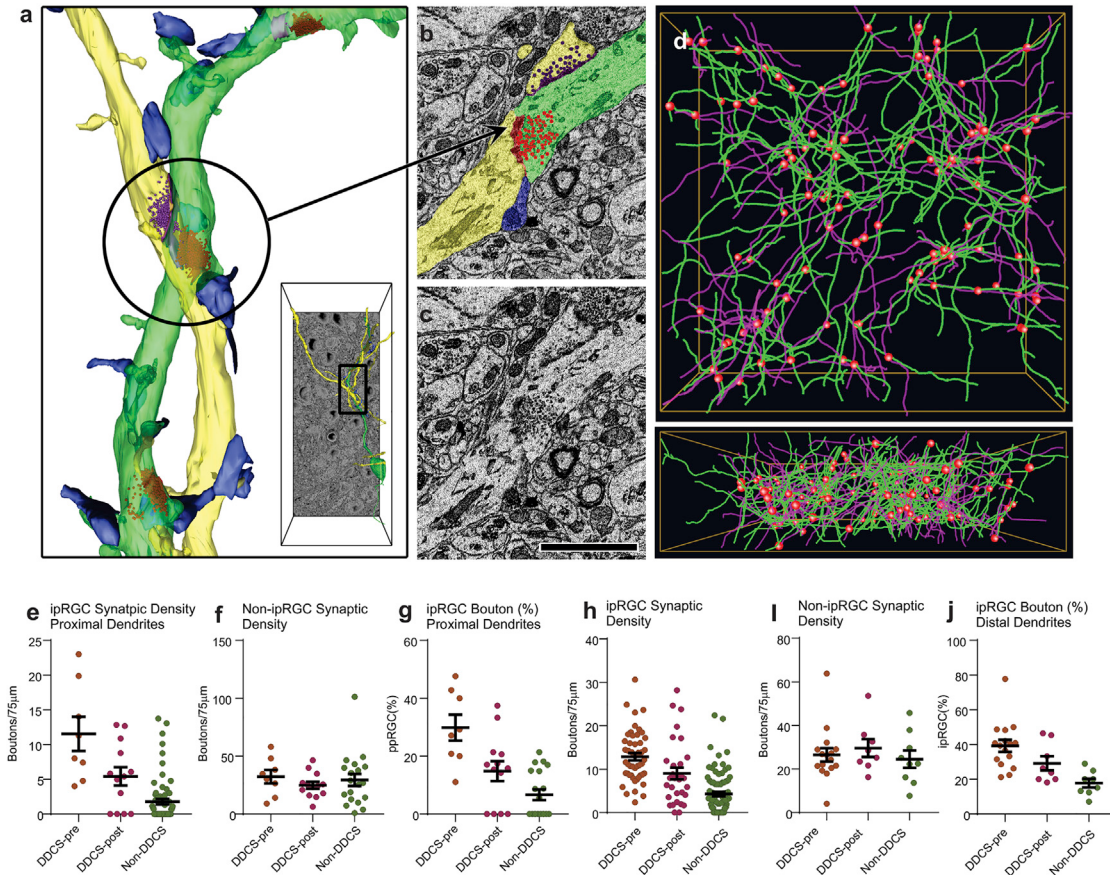
All data are from tissues collected from one mouse. Scale bar, 1 μm .

See also Figure S6.

volume. Electron microscopy images of each of the 737 dendrites in every imaged plane (a total of more than 100,000 dendrite images) were visually inspected for the presence of DDCSs. Dendrites that formed synapses on another dendrite are referred to as “DDCS-pre” dendrites (Figures 6A–6C; Video S6), and the post-synaptic dendrites are referred to as “DDCS-post” dendrites (Figures 6A–6C; Video S6). We found a total of 85 DDCS dendrites interconnected at 65 DDCSs.

Given that only ~10% of these 737 dendrites were DDCS-pre or DDCS-post, if DDCSs formed randomly, then we would expect only 1% or 7 dendrites to be both DDCS-pre and DDCS-post. However, 15 dendrites had both a pre- and postsynaptic site, suggesting that a dendrite or neuron that makes a DDCS is more likely to receive a DDCS and vice versa. We therefore followed these 65 DDCSs in both the retrograde and anterograde direction, searching for additional DDCSs. Each newly identified DDCS was then followed until we exhausted our search. We identified 112 DDCS sites that connected a total of 136 DDCS dendrites (Figure 6D), of which 76 were DDCS-pre, 91 were DDCS-post, and 31 belonged to both groups. Because ~10% of randomly selected SCN dendrites were DDCS+, and there were an estimated 1,535 dendrites in the volume, we believe that the network of 136 dendrites represented majority of the expected ~155 DDCSs within the SCN volume (Figure S7; Video S6).

Overall, the number of DDCS-pre and DDCS-post sites per length of dendrite was the same, with 2.49 ± 0.19 presynaptic sites per 100 μm dendritic length ($n = 76$) and 2.51 ± 0.17 post-synaptic sites per 100 μm dendritic length ($n = 91$). Because a fraction of surveyed dendrite segments within the imaged volume were shorter than the average distance between consecutive DDCSs, after correcting for false negatives, we concluded that 47.7% of all DDCS-post dendrites were also presynaptic at at least one site and that 57.1% of all DDCS-pre dendrites were synapsed upon at least once by a DDCS. Given that dendrites with DDCSs account for only a small fraction of randomly selected dendrites (the overall proportion of each in the tissue as a whole was estimated to be 7.8%), the disproportionate overlap between these two groups suggests a high degree of selective network connectivity.

**Figure 6. Dendrodendritic Synaptic Network in the SCN**

(A) 3D view of two SCN dendrites (green and yellow) making a reciprocal chemical synapse with presynaptic vesicles (red and purple) and ipRGC boutons (blue). (B and C) Pseudo-colored (B) and original (C) 2D view of reciprocal DDCSs between two SCN dendrites and an ipRGC bouton. (D) 3D view of the DDCS network with 136 dendrites (presynaptic in green and postsynaptic in purple) connected at 112 synapses (red). (E) ipRGC synaptic density on proximal dendrites. (F) Proximal non-ipRGC synaptic density. (G) ipRGC boutons (percent) on proximal regions. (H) ipRGC synaptic density on distal dendrites. (I) Distal non-ipRGC synaptic density. (J) ipRGC boutons (percent) on distal regions.

All statistical tests and significant differences between groups are shown in Table 3 and Table S1. All data are from tissues collected from one mouse. Scale bar, 2 μ m. See also Figure S7.

DDCS Dendrites in the SCN Receive Relatively More ipRGC Input Than Non-DDCS Dendrites

In proximal segments, DDCS-pre dendrites received the highest number of ipRGC synapses per 75 μ m dendritic length; DDCS-post dendrites received less than half, and non-DDCS dendrites received the fewest (Figure 6E; Table 3). In contrast, non-ipRGC synapses were nearly uniformly distributed among the proximal segments of DDCS-pre, DDCS-post, and non-DDCS dendrites (Figure 6F). In other words, DDCS-pre dendrites had a greater proportion of ipRGC synapses in proximal dendrites: DDCS-pre ($29.85\% \pm 4.48\%$, n = 8), DDCS-post ($14.84\% \pm 3.42\%$, n = 13), and non-DDCS ($6.70\% \pm 1.85$; n = 19) (Figure 6G; Table 3; Table S1).

Distal dendrites with DDCS-pre dendrites also received the highest level of ipRGC synapses per 75 μ m dendritic length,

followed by DDCS-post dendrites, and non-DDCS dendrites (Figure 6H). Similar to proximal dendrites, in distal segments, non-ipRGC boutons did not show any preference for DDCS dendrites (Figure 6I). Accordingly, in distal segments, DDCS⁺ dendrites were enriched for ipRGC inputs: DDCS-pre ($39.27\% \pm 3.40\%$, n = 16), DDCS-post ($29.19\% \pm 3.62\%$, n = 10), and non-DDCS ($18.57\% \pm 2.37$, n = 9) (Figure 6J; Table 3). In summary, the DDCS network received a disproportionately higher fraction of axo-dendritic synapses from ipRGCs.

DISCUSSION

ipRGCs have been classified into up to 6 different subtypes based on their dendritic arbors in the retina. However, there is no conclusive evidence that any subtype specifically and

Table 3. Quantitative Assessment of ipRGC Boutons in the Proximal and Distal SCN Dendrites in Relation to the Presence of DDCS

Features	DDCS-Pre	DDCS-Post	Non-DDCS
Proximal Dendrites			
ipRGC synapses/75 μm dendritic length	11.55 ± 2.46, n = 8 ^a	5.42 ± 1.32, n = 13 ^b	1.78 ± 0.39, n = 67 ^c
Non-ipRGC synapses/75 μm dendritic length	32.33 ± 5.76, n = 8, ns	24.84 ± 3.00, n = 13, ns	29.49 ± 5.28, n = 19, ns
Percentage of synapses that are ipRGC positive	29.85% ± 4.48%, n = 8 ^a	14.84% ± 3.42%, n = 13 ^b	6.70% ± 1.85, n = 19 ^b
Distal Dendrites			
ipRGC synapses/75 μm dendritic length	12.88 ± 1.08, n = 33 ^a	9.02 ± 1.4, n = 30 ^b	4.29 ± 0.50, n = 88 ^c
Non-ipRGC synapses/75 μm dendritic length	26.52 ± 3.11, n = 16, ns	29.63 ± 4.15, n = 10, ns	24.53 ± 3.97, n = 9, ns
Percentage of synapses that are ipRGC positive	39.27% ± 3.40%, n = 16 ^a	29.19% ± 3.62%, n = 10 ^{a,b}	17.77% ± 2.52, n = 9 ^{b,c}

Groups that are not statistically different share the same letter. ns, not significant. A summary of statistical analyses is shown in Table S1.

^aipRGC boutons exhibit region-specific specialization in five different retinofugal brain nuclei examined.

^bFeatures of ipRGC axonal arbors and synapses in the SCN and OPN.

^cQuantitative assessment of ipRGC boutons in proximal and distal SCN dendrites in relation to the presence of DDCSs.

exclusively targets any brain region. By quantitatively determining the ultrastructural features of ipRGC synaptic contacts within these volumes, we discovered salient target-specific synaptic properties of ipRGCs. First, the axonal arbors of ipRGCs show brain region-specific specializations with respect to axonal branching pattern and synaptic bouton morphology and a preference for synapsing on proximal or distal dendrites. Second, in contrast to bipolar cells in the retina, which receive input exclusively from rod/cone photoreceptors, none of the volumes analyzed revealed evidence of dedicated cell types that receive input exclusively from ipRGCs. In the OPN and SCN, which exclusively receive retina input through ipRGCs, ipRGC input accounted for less than 20% of all axo-dendritic inputs. Third, although there was no evidence of a cell type that receives synaptic input exclusively from ipRGCs, in the SCN we were surprised to discover a small subset of neurons that may locally and directly inhibit one another because their dendrites are interconnected via DDCSs. These DDCS-bearing neurons of the SCN receive a disproportionately larger share of ipRGC synapses, perhaps providing a mechanism to coordinate and synchronize the dendritic depolarization states for dendrites of SCN neurons that are most strongly targeted for ipRGC input.

Genetically Encoded Electron Microscopy Tags and SBEM for Focused Characterization of Synaptic Architecture

It is becoming increasingly clear that genetically defined neuron types often project to or receive input from more than one brain region, raising the question of whether a particular type of neuron makes similar connections with all recipient neurons or whether the connections are specialized for each target neuron or brain region. Conventional wisdom has been that each type of neuron connects to all of its target neurons using a signature type of synaptic contact, although some reports with light microscopy techniques have suggested that certain neurons may have target-specific synaptic properties. This gap in knowledge exists because current technologies for high-resolution circuit mapping are often volumetrically limited because of physical restrictions imposed by large-scale electron microscopy techniques or computationally limited because of challenges associated with processing and analyzing extremely large voxel volumes of

data. In this study, we address these critical technical and analytical barriers.

First, the use of a genetically encoded electron microscopy tag to completely label the axonal fields of a well-defined type of neuron and collecting focused SBEM image stacks from different brain regions separated from one another by several millimeters allowed us to circumvent the volume limitation challenge.

Second, a membrane-tethered version of the miniSOG reporter facilitated automatic segmentation, followed by a manual correction to accelerate image processing. At least in the SCN, all 88 manually traced axon arbors were detected by this automatic segmentation approach. However, we also noticed limitations of the automatic segmentation algorithm we employed, specifically when other features, including myelinated axons or capillaries, interfered with the analysis and increased false positives. Furthermore, myelinated miniSOG⁺ ipRGC axons in the ON were often devoid of the miniSOG label at the nodes of Ranvier. Nevertheless, this limitation did not prevent us from using automatic segmentation to verify uniform labeling and photo-oxidation of the sample prior to investing significant human resources (computational and manual tracing) to annotate the image. This labeling strategy was also aided by combining X-ray micro-computed tomography (microCT) to “visualize” a larger sample, enabling selection of a sub-region with suitable staining and location for subsequent SBEM imaging (Bushong et al., 2014). Finally, the use of simple, unbiased random sampling techniques enabled quantitative analyses of ultrastructural features without complete reconstruction of imaged volumes. Using the grid-based method to randomly sample ultrastructural features of interest (e.g., axons, boutons, or dendrites) and random column-based sampling to count or reconstruct features of interest will accelerate quantitative analyses of SBEM datasets with a judicious allocation of resources.

ipRGC Axons within Different Brain Regions Have Structurally Distinct Synapses

Although LM studies have indicated that genetically or physiologically distinct neurons (e.g., RGCs [Bhide and Frost, 1991] or geniculocortical neurons [Humphrey et al., 1985; Sur et al., 1987; Tamamaki et al., 1995]) may have heterogeneous terminal

fields, quantitative assessment of terminal field architecture or synaptic features at an ultrastructural level is lacking. In this study, we showed that ipRGC axons have both common and specific terminal field architectures in different brain regions and that these differences may partially explain their functional specialization.

All ipRGCs express *Opn4* and are considered glutamatergic. The M1 subtype, which has been extensively studied, expresses the highest levels of melanopsin protein and sends axonal projections to at least a dozen brain regions and sparse projections to the dorsomedial aspect of the dLGN (Hattar et al., 2006). Therefore, all brain targets imaged in this study (the SCN, vLGN, IGL, OPN, and dLGN) receive at least some M1 projections. However, the visual responses mediated by these brain regions vary widely in terms of threshold sensitivity, speed, and accuracy.

ipRGC axons and their synapses were clearly distinct from those of rod/cone photoreceptors. Unlike rod/cone photoreceptors, we found that all ipRGC axons were myelinated in the ON. Myelinated ipRGC fibers were also found in the IGL, dLGN, vLGN, and OPN, whereas collaterals that reached the SCN were unmyelinated, reflecting target-specific differences in myelination of axon collaterals that subserve different visual responses. Speed and synchrony of action potential transmission may not be necessary for the relatively slow photoentrainment of the SCN circadian clock to ambient lighting. In contrast, rapid adaptation of the pupil to ambient light levels or brightness perception of the visual scene requires much faster responses, which are ensured by maintaining myelination of ipRGC axons that extend to regions such as the OPN and LGN.

Unlike rod/cone photoreceptors, which predominantly use terminal synapses, ipRGC axons within the five brain regions examined predominantly use *en passant* synapses. This is in contrast to earlier electron microscopy studies in the SCN of rodents, in which all retinal afferents were labeled with horseradish peroxidase. Studies of individual electron microscopy images assumed that retinal synapses in the SCN were predominantly terminal synapses (Güldner, 1978a).

The observed heterogeneity in ipRGC axonal arbors within five different brain regions is remarkable. Based on size, synaptic properties, and function, glutamatergic boutons are typically of two types: large class 1 boutons ($>2 \mu\text{m}^2$ cross-sectional area) and small class 2 boutons ($<1 \mu\text{m}^2$ cross-sectional area) (Petrof and Sherman, 2013). Class 1 boutons that produce large excitatory postsynaptic potentials (EPSPs) are considered drivers, whereas class 2 boutons produce smaller EPSPs and mostly play modulatory roles. As seen with other RGCs (Hammer et al., 2015), ipRGC boutons in the dLGN were very large with multiple spine intrusions, meeting the criteria for class 1 boutons. Large ipRGC boutons in the dLGN ensure higher information flow through these synapses; however, the low density of ipRGC boutons suggests that they may only modulate the activity of recipient dLGN neurons. The majority of ipRGC boutons in the OPN also met the size criteria for class 1 boutons. ipRGC boutons in the OPN with high mitochondrial content and fewer than 2 synapses devoted more resources per synapse. Like other class 1 boutons (Petrof and Sherman, 2013), these ipRGC boutons in the OPN were on relatively thick axons and preferen-

tially formed synapses on proximal dendrites or the somata of recipient cells, where they would be more likely to drive action potentials. The anatomical and synaptic properties of ipRGC boutons in the OPN enable this input to drive (rather than modulate) rapid pupil constriction in response to light.

Extensive branching of ipRGC axonal arbors in the OPN can account for the relative sparsity of neuronal somata in the OPN and for the preference of ipRGC boutons to synapse on somata and proximal dendrites. Such a branching pattern ensures that a single ipRGC axon synapses onto multiple OPN neurons and, conversely, that individual OPN neurons receive input from multiple ipRGCs, thus endowing individual OPN neurons with larger receptive fields. Although ipRGC axonal arbors in the SCN were less branched, they still followed a similar synaptic pattern in that individual SCN neurons received input from multiple ipRGCs, and individual ipRGCs sent input to multiple SCN neurons. A high density of neurons in the SCN (relative to the OPN), coupled with the preference of ipRGC boutons to synapse onto distal dendrites in the SCN, implies that ipRGC axons do not have to branch too much to find a distal dendrite.

ipRGC boutons in the SCN are distinct from those in the OPN or dLGN. Their smaller size, thinner axon diameter, and preference for distal dendrites are characteristic features of class 2 glutamatergic boutons (Petrof and Sherman, 2013). However, earlier studies predicted most retinal afferent synapses in the SCN to be larger in size and clustered in glomerular structures (Card and Moore, 1991). A limited number of electron microscopy images of the SCN and inherent bias toward characterizing larger synapses might have led to this conclusion. The preference of ipRGC axons to synapse on distal dendrites of SCN neurons is in agreement with earlier studies that found sparse axo-somatic synapses by retina afferents in the SCN (Card and Moore, 1991; Güldner, 1976, 1978b). The M1 subtype of ipRGCs is known to send axon collaterals to both the SCN and OPN (Fernandez et al., 2016). Although it was never ruled out that both classes of glutamatergic boutons may be present on the same neuron (Petrof and Sherman, 2013), the discovery of class 2 glutamatergic ipRGC boutons in the SCN and class 1 boutons on ipRGC collaterals in the OPN is such an example. Class 2 boutons in the SCN are appropriate for photoentrainment of the SCN clocks. Because synaptic potentials decrease as they propagate through dendrites toward the soma (Häusser et al., 2000; Magee, 2000; Williams and Stuart, 2002), individual class 2 ipRGC boutons on distal SCN dendrites may have negligible effects on neuron function in the SCN. However, this synaptic architecture potentially serves two purposes. Distal synapses, when activated simultaneously, can synergistically add synaptic potential and thereby better serve as coincidence detectors (Williams and Stuart, 2002). Because individual SCN neurons receive input from multiple ipRGCs, such a coincidence detector function of ipRGC synapses may ensure that SCN pacemaker neurons receive light information only when a large visual field is illuminated. Second, ipRGC boutons account for less than 15% of all incoming synapses on SCN dendrites. Therefore, SCN dendrites may be a site for dendritic computation (London and Häusser, 2005; Magee, 2000), in which direct ipRGC input is weighted against afferent inputs from the IGL, raphe, paraventricular thalamus (PVT), and local input to modulate the function

of SCN neurons. At least in mice, the relative strength of direct ipRGC input and indirect light input via the IGL has been postulated to set the day or night preference of locomotor activity (Delogu et al., 2012).

ipRGCs Preferentially (Not Exclusively) Make Synapses with DDCS-Pre SCN Dendrites

The data collected in this study indicate some synaptic specializations among SCN neurons. Even within the ventral SCN, which is presumed to be enriched for ipRGC input, nearly half of the neurons did not receive any ipRGC input on their somata or proximal dendrites, whereas almost all distal SCN dendrites received ipRGC input.

We found that ~10% of SCN dendrites form DDCSs at a frequency of ~2 DDCSs per 100 μm of dendrite, which is in alignment with prior predictions (Güldner, 1976). Although the DDCSs have been described previously, the current study offers an ultrastructural framework to clarify the relevance of DDCSs to SCN function. The dendrites that are presynaptic to a DDCS were remarkably enriched in ipRGC inputs. On these pre-DDCS dendrites, ipRGC synapses accounted for as much as 40% or 30% of all synapses within the distal and proximal regions, respectively. In contrast, for non-DDCS dendrites, ipRGCs accounted for 19% or 7% of all synapses within the distal and proximal regions, respectively.

A small number of SCN neurons connected through the DDCS network and receiving a high number of ipRGC inputs may help to explain a functional feature of the SCN that has been postulated for a long time but lacked physical proof. Multiple studies over the past 5 decades have pointed to the existence of a core set of specialized neurons within the SCN that receive light input from the retina and serve as critical nodes in sustaining network-level circadian oscillation. Upon desynchronization of SCN neurons *ex vivo*, a smaller subset of SCN neurons in the ventral SCN spontaneously resynchronize much earlier than the rest of the SCN (Abel et al., 2016). This led to the hypothesis that SCN neurons behave like a small-world network in which a small subset of ventral SCN neurons forms a functional network. Parallel studies of light pulse-induced acute expression of the immediate early gene *c-fos* or acute upregulation of Per1 and Per2 also led to the hypothesis that ventral SCN neurons act as retinorecipient gate neurons (Karat-soreos et al., 2004; Yan and Silver, 2002), receiving ocular light signals and transmitting these signals to the rest of the SCN. These two independent lines of investigation into photoresponses and SCN network architecture had each predicted that a small subset of ventral SCN neurons may form a tighter network.

The nature of this SCN network has remained elusive, and results from independent studies have pointed to redundant mechanisms. Although dye coupling studies have indicated the presence of gap junctions and electrical coupling of SCN neurons (Colwell, 2000), there are also data supporting the presence of neurotransmitter (VIP)-mediated chemical synapses that mediate coupling among a small subset of ventral SCN neurons (Aton et al., 2005). The labeling and imaging method used here could not resolve electrical connections, so we could not place electrical synapses within the observed connectome. However,

mutant mice that lack connexins, or those lacking VIP or the VIP receptor, do not show complete abolition of coupling (Herzog et al., 2017). Similarly, a recent study of the ontogeny of SCN synchrony indicated that such synchrony appears prior to the expression of VIP (Carmona-Alcocer et al., 2018). Therefore, it is parsimonious to conclude that the DDCS network, with its high preference for ipRGC input, offers a plausible network motif within the SCN to enhance the effect of ipRGC signals, thus achieving a strong response within this nucleus to light input.

DDCSs are GABAergic inhibitory synapses and have been well characterized in the olfactory bulb (Rall et al., 1966) where they serve two major functions that are relevant to the SCN. Inhibitory DDCSs in the olfactory bulb use lateral inhibition to better discriminate between different olfactory stimuli (Yokoi et al., 1995). DDCS networks have been postulated to synchronize neurons to produce gamma oscillations and thalamic spindle synchronization in the olfactory bulb and in the reticular thalamic nucleus, respectively (Deschênes et al., 1985; Lagier et al., 2007). Unlike these oscillations, circadian oscillations are cell autonomous. Therefore, DDCSs in the SCN are not involved in generating circadian oscillations, but they can play a role in synchronizing SCN neurons.

The proximity of ipRGC inputs to inhibitory DDCSs also offers a potential mechanism for discriminating synaptic input to the SCN network and increasing the preference for light as the dominant entraining stimulus or zeitgeber. An alternative explanation for ipRGC targeting of DDCS dendrites is to help the SCN network resist large phase shifts in response to an ocular light pulse, whereas comparable perturbation of individual SCN neuron would trigger a phase shift. Although we could not fully reconstruct the network of SCN neurons that are connected through DDCSs, in the olfactory bulb (Shepherd et al., 2007) and cortex (Le Magueresse et al., 2011), such neurons are typically axonless, small neurons. Thus, the dendrites contain both input and release sites. Sensory input, such as an olfactory stimulus, enhances the number of small, axonless neurons in the mouse cortex (Le Magueresse et al., 2011), offering a mechanism by which sensory inputs early in life influence local network structure in the recipient brain region. The function of the rodent SCN is also affected by light exposure during early postnatal life. This effect depends on GABAergic signaling (Azzi et al., 2017), but the underlying cellular network is currently unknown. Together, the data presented here form a foundation for future perturbation experiments as well as physiological and computational work to test the role of DDCS-preferred ipRGC input in SCN function and in helping the network calibrate light input.

STAR★METHODS

Detailed methods are provided in the online version of this paper and include the following:

- KEY RESOURCES TABLE
- LEAD CONTACT AND MATERIALS AVAILABILITY
- EXPERIMENTAL MODEL AND SUBJECT DETAILS
 - Animals

METHOD DETAILS

- Vector Construction
- Vector Injection
- Circadian Wheel Running
- Immunofluorescence and Confocal Microscopy
- Tissue Preparation, Fluorescence Imaging, and Photo-oxidation of Mouse Retina and Brain
- SBEM Preparation and Imaging
- Electron Tomography
- Manual Segmentation
- Proximal to distal synaptic density nonlinear regression
- Automatic Segmentation

QUANTIFICATION AND STATISTICAL ANALYSIS**DATA AND CODE AVAILABILITY****SUPPLEMENTAL INFORMATION**

Supplemental Information can be found online at <https://doi.org/10.1016/j.celrep.2019.09.006>.

ACKNOWLEDGMENTS

The research was supported by NIH NEI grant EY 016807 (to S.P.), NIH NIGMS P41GM103412 and RO1 GM086197 (to M.H.E.), and NINDS RO1 NS027177 (to M.H.E.). We also received support from NIH R01GM086197. We thank Dr. David O’Keefe for help with preparing the manuscript and Daniela Boassa, Hiroyuki Hakozaki, Willy Wong, and Andrea Thor for technical support.

AUTHOR CONTRIBUTIONS

M.H.E. played a key role in SBEM data collection for the project, and S. Panda played a key role in the biology and data analyses of this project. Quantitative Data Analyses, K.-Y.K., L.C.R., A.J.P., and S. Phan; Resources, M.H.E. and S. Panda; Validation, H.L., M. Hatori, V.L.-R., M.A.E., and A.J.P.; Investigation, K.-Y.K., L.C.R., Y.H.L., A.J.P., L.S.M., S. Phan, E.A.B., S.J., S.A.P., M. Hirayama, S.Y., and S. Panda; Visualization, K.-Y.K., L.C.R., Y.H.L., and A.J.P.; Methodology, K.-Y.K., S.P., E.A.B., T.J.D., and M.H.E.; Writing – Original Draft, K.-Y.K., L.C.R., Y.H.L., S. Panda, M.H.E.; Writing, K.-Y.K., L.C.R., M.H.E., and S. Panda; Review and Editing, K.-Y.K., L.C.R., T.J.D., E.A.B., M.H.E., and S. Panda.

DECLARATION OF INTERESTS

S. Panda is the author of the book “The Circadian Code.”

Received: June 23, 2018

Revised: July 1, 2019

Accepted: September 4, 2019

Published: October 15, 2019

REFERENCES

- Abel, J.H., Meeker, K., Granados-Fuentes, D., St John, P.C., Wang, T.J., Bales, B.B., Doyle, F.J., 3rd, Herzog, E.D., and Petzold, L.R. (2016). Functional network inference of the suprachiasmatic nucleus. *Proc. Natl. Acad. Sci. USA* **113**, 4512–4517.
- Anderson, J.R., Wilcox, M.J., Wade, P.R., and Barrett, S.F. (2003). Segmentation and 3D reconstruction of biological cells from serial slice images. *Biomed. Sci. Instrum.* **39**, 117–122.
- Anderson, J.R., Jones, B.W., Watt, C.B., Shaw, M.V., Yang, J.H., Demill, D., Lauritzen, J.S., Lin, Y., Rapp, K.D., Mastronarde, D., et al. (2011). Exploring the retinal connectome. *Mol. Vis.* **17**, 355–379.
- Atasoy, D., Betley, J.N., Li, W.P., Su, H.H., Sertel, S.M., Scheffer, L.K., Simpson, J.H., Fetter, R.D., and Sternson, S.M. (2014). A genetically specified connectomics approach applied to long-range feeding regulatory circuits. *Nat. Neurosci.* **17**, 1830–1839.
- Aton, S.J., Colwell, C.S., Harmar, A.J., Waschek, J., and Herzog, E.D. (2005). Vasoactive intestinal polypeptide mediates circadian rhythmicity and synchrony in mammalian clock neurons. *Nat. Neurosci.* **8**, 476–483.
- Azzi, A., Evans, J.A., Leise, T., Myung, J., Takumi, T., Davidson, A.J., and Brown, S.A. (2017). Network Dynamics Mediate Circadian Clock Plasticity. *Neuron* **93**, 441–450.
- Berson, D.M., Dunn, F.A., and Takao, M. (2002). Phototransduction by retinal ganglion cells that set the circadian clock. *Science* **295**, 1070–1073.
- Berson, D.M., Castrucci, A.M., and Provencio, I. (2010). Morphology and mosaics of melanopsin-expressing retinal ganglion cell types in mice. *J. Comp. Neurol.* **518**, 2405–2422.
- Blidie, P.G., and Frost, D.O. (1991). Stages of growth of hamster retinofugal axons: implications for developing axonal pathways with multiple targets. *J. Neurosci.* **11**, 485–504.
- Briggman, K.L., and Bock, D.D. (2012). Volume electron microscopy for neuronal circuit reconstruction. *Curr. Opin. Neurobiol.* **22**, 154–161.
- Brown, T.M., Gias, C., Hatori, M., Keding, S.R., Semo, M., Coffey, P.J., Gigg, J., Piggins, H.D., Panda, S., and Lucas, R.J. (2010). Melanopsin contributions to irradiance coding in the thalamo-cortical visual system. *PLoS Biol.* **8**, e1000558.
- Bushong, E.A., Johnson, D.D., Kim, K.Y., Terada, M., Hatori, M., Peltier, S.T., Panda, S., Merkle, A., and Ellisman, M.H. (2014). X-Ray Microscopy as an Approach to Increasing Accuracy and Efficiency of Serial Block-Face Imaging for Correlated Light and Electron Microscopy of Biological Specimens. *Microsc. Microanal.* **21**, 231–238.
- Card, J.P., and Moore, R.Y. (1991). The organization of visual circuits influencing the circadian activity of the suprachiasmatic nucleus. In *Suprachiasmatic Nucleus: the Mind’s Clock*, D.C. Klein, R.Y. Moore, and S. Reppert, eds. (Oxford University Press), pp. 51–76.
- Cardin, J.A., Carlén, M., Meletis, K., Knoblich, U., Zhang, F., Deisseroth, K., Tsai, L.H., and Moore, C.I. (2009). Driving fast-spiking cells induces gamma rhythm and controls sensory responses. *Nature* **459**, 663–667.
- Carmona-Alcocer, V., Abel, J.H., Sun, T.C., Petzold, L.R., Doyle, F.J., 3rd, Simms, C.L., and Herzog, E.D. (2018). Ontogeny of circadian rhythms and synchrony in the suprachiasmatic nucleus. *J. Neurosci.* **38**, 1326–1334.
- Castel, M., and Morris, J.F. (2000). Morphological heterogeneity of the GABAergic network in the suprachiasmatic nucleus, the brain’s circadian pacemaker. *J. Anat.* **196**, 1–13.
- Castel, M., Morris, J., and Belenky, M. (1996). Non-synaptic and dendritic exocytosis from dense-cored vesicles in the suprachiasmatic nucleus. *NeuroReport* **7**, 543–547.
- Colwell, C.S. (2000). Rhythmic coupling among cells in the suprachiasmatic nucleus. *J. Neurobiol.* **43**, 379–388.
- Deerinck, T.J., Bushong, E., Thor, A., and Ellisman, M.H. (2010). NCMIR methods for 3D EM: A new protocol for preparation of biological specimens for serial block-face SEM. SBEM Protocol v7_01_10.. <https://ncmir.ucsd.edu/sbem-protocol>
- Delogu, A., Sellers, K., Zagoraiou, L., Bocianowska-Zbrog, A., Mandal, S., Giménez, J., Rubenstein, J.L.R., Sugden, D., Jessell, T., and Lumsden, A. (2012). Subcortical visual shell nuclei targeted by ipRGCs develop from a Sox14+-GABAergic progenitor and require Sox14 to regulate daily activity rhythms. *Neuron* **75**, 648–662.
- Denk, W., and Horstmann, H. (2004). Serial block-face scanning electron microscopy to reconstruct three-dimensional tissue nanostructure. *PLoS Biol.* **2**, e329.
- Deschénes, M., Madariaga-Domich, A., and Steriade, M. (1985). Dendrodendritic synapses in the cat reticularis thalami nucleus: a structural basis for thalamic spindle synchronization. *Brain Res.* **334**, 165–168.

- Fernandez, D.C., Chang, Y.T., Hattar, S., and Chen, S.K. (2016). Architecture of retinal projections to the central circadian pacemaker. *Proc. Natl. Acad. Sci. USA* **113**, 6047–6052.
- Güldner, F.H. (1976). Synaptology of the rat suprachiasmatic nucleus. *Cell Tissue Res.* **165**, 509–544.
- Güldner, F.H. (1978a). Synapses of optic nerve afferents in the rat suprachiasmatic nucleus. I. Identification, qualitative description, development and distribution. *Cell Tissue Res.* **194**, 17–35.
- Güldner, F.H. (1978b). Synapses of optic nerve afferents in the rat suprachiasmatic nucleus. II. Structural variability as revealed by morphometric examination. *Cell Tissue Res.* **194**, 37–54.
- Güldner, F.H., and Wolff, J.R. (1974). Dendro-dendritic synapses in the suprachiasmatic nucleus of the rat hypothalamus. *J. Neurocytol.* **3**, 245–250.
- Hammer, S., Monavarfeshani, A., Lemon, T., Su, J., and Fox, M.A. (2015). Multiple Retinal Axons Converge onto Relay Cells in the Adult Mouse Thalamus. *Cell Rep.* **12**, 1575–1583.
- Hatori, M., and Panda, S. (2010). The emerging roles of melanopsin in behavioral adaptation to light. *Trends Mol. Med.* **16**, 435–446.
- Hatori, M., Le, H., Vollmers, C., Keding, S.R., Tanaka, N., Buch, T., Waisman, A., Schmedt, C., Jegla, T., and Panda, S. (2008). Inducible ablation of melanopsin-expressing retinal ganglion cells reveals their central role in non-image forming visual responses. *PLoS ONE* **3**, e2451.
- Hattar, S., Liao, H.W., Takao, M., Berson, D.M., and Yau, K.W. (2002). Melanopsin-containing retinal ganglion cells: architecture, projections, and intrinsic photosensitivity. *Science* **295**, 1065–1070.
- Hattar, S., Kumar, M., Park, A., Tong, P., Tung, J., Yau, K.W., and Berson, D.M. (2006). Central projections of melanopsin-expressing retinal ganglion cells in the mouse. *J. Comp. Neurol.* **497**, 326–349.
- Häusser, M., Spruston, N., and Stuart, G.J. (2000). Diversity and dynamics of dendritic signaling. *Science* **290**, 739–744.
- Helmstaedter, M., Briggman, K.L., Turaga, S.C., Jain, V., Seung, H.S., and Denk, W. (2013). Connectomic reconstruction of the inner plexiform layer in the mouse retina. *Nature* **500**, 168–174.
- Herzog, E.D., Hermanstyne, T., Smyllie, N.J., and Hastings, M.H. (2017). Regulating the Suprachiasmatic Nucleus (SCN) Circadian Clockwork: Interplay between Cell-Autonomous and Circuit-Level Mechanisms. *Cold Spring Harb. Perspect. Biol.* **9**, a027706.
- Humphrey, A.L., Sur, M., Uhlrich, D.J., and Sherman, S.M. (1985). Termination patterns of individual X- and Y-cell axons in the visual cortex of the cat: projections to area 18, to the 17/18 border region, and to both areas 17 and 18. *J. Comp. Neurol.* **233**, 190–212.
- Joesch, M., Mankus, D., Yamagata, M., Shahbazi, A., Schalek, R., Suissa-Peleg, A., Meister, M., Lichtman, J.W., Scheirer, W.J., and Sanes, J.R. (2016). Reconstruction of genetically identified neurons imaged by serial-section electron microscopy. *eLife* **5**, e15015.
- Karatsoreos, I.N., Yan, L., LeSauter, J., and Silver, R. (2004). Phenotype matters: identification of light-responsive cells in the mouse suprachiasmatic nucleus. *J. Neurosci.* **24**, 68–75.
- Kim, J.S., Greene, M.J., Zlateski, A., Lee, K., Richardson, M., Turaga, S.C., Purcaro, M., Balkam, M., Robinson, A., Behabadi, B.F., et al.; EyeWires (2014). Space-time wiring specificity supports direction selectivity in the retina. *Nature* **509**, 331–336.
- Kofuji, P., Mure, L.S., Massman, L.J., Purrier, N., Panda, S., and Engeland, W.C. (2016). Intrinsic Photosensitive Retinal Ganglion Cells (ipRGCs) Are Necessary for Light Entrainment of Peripheral Clocks. *PLoS ONE* **11**, e0168651.
- Kremer, J.R., Mastronarde, D.N., and McIntosh, J.R. (1996). Computer visualization of three-dimensional image data using IMOD. *J. Struct. Biol.* **116**, 71–76.
- Lagier, S., Panzanelli, P., Russo, R.E., Nissant, A., Bathellier, B., Sassoè-Pognetto, M., Fritschy, J.M., and Lledo, P.M. (2007). GABAergic inhibition at dendrodendritic synapses tunes gamma oscillations in the olfactory bulb. *Proc. Natl. Acad. Sci. USA* **104**, 7259–7264.
- Lawrence, A., Bouwer, J.C., Perkins, G., and Ellisman, M.H. (2006). Transform-based backprojection for volume reconstruction of large format electron microscope tilt series. *J. Struct. Biol.* **154**, 144–167.
- Le Magueresse, C., Alfonso, J., Khodosevich, K., Arroyo Martín, A.A., Bark, C., and Monyer, H. (2011). “Small axonless neurons”: postnatally generated neocortical interneurons with delayed functional maturation. *J. Neurosci.* **31**, 16731–16747.
- London, M., and Häusser, M. (2005). Dendritic computation. *Annu. Rev. Neurosci.* **28**, 503–532.
- Magee, J.C. (2000). Dendritic integration of excitatory synaptic input. *Nat. Rev. Neurosci.* **1**, 181–190.
- Moore, R.Y., Speh, J.C., and Leak, R.K. (2002). Suprachiasmatic nucleus organization. *Cell Tissue Res.* **309**, 89–98.
- Mure, L.S., and Panda, S. (2012). Fear of the light or need for action: the IGL will judge. *Neuron* **75**, 546–548.
- Mure, L.S., Hatori, M., Zhu, Q., Demas, J., Kim, I.M., Nayak, S.K., and Panda, S. (2016). Melanopsin-Encoded Response Properties of Intrinsically Photosensitive Retinal Ganglion Cells. *Neuron* **90**, 1016–1027.
- Palay, S.L., and Palade, G.E. (1955). The fine structure of neurons. *J. Biophys. Biochem. Cytol.* **1**, 69–88.
- Perez, A.J., Seyedhosseini, M., Deerinck, T.J., Bushong, E.A., Panda, S., Tasdizen, T., and Ellisman, M.H. (2014). A workflow for the automatic segmentation of organelles in electron microscopy image stacks. *Front. Neuroanat.* **8**, 126.
- Petroff, I., and Sherman, S.M. (2013). Functional significance of synaptic terminal size in glutamatergic sensory pathways in thalamus and cortex. *J. Physiol.* **591**, 3125–3131.
- Phan, S., Boassa, D., Nguyen, P., Wan, X., Lanman, J., Lawrence, A., and Ellisman, M.H. (2017). 3D reconstruction of biological structures: automated procedures for alignment and reconstruction of multiple tilt series in electron tomography. *Adv. Struct. Chem. Imaging* **2**, 8.
- Powers, D.M.W. (2011). Evaluation: From precision, recall, and F-measure to ROC, informedness, markedness and correlation. *J. Mach. Learn. Technol.* **2**, 37–63.
- Rall, W., Shepherd, G.M., Reese, T.S., and Brightman, M.W. (1966). Dendrodendritic synaptic pathway for inhibition in the olfactory bulb. *Exp. Neurol.* **14**, 44–56.
- Seyedhosseini, M., Sajjadi, M., and Tasdizen, T. (2013). Image Segmentation with Cascaded Hierarchical Models and Logistic Disjunctive Normal Networks. *Proc. IEEE Int. Conf. Comput. Vis.* **2013**, 2168–2175.
- Shepherd, G.M. (2009). Symposium overview and historical perspective: dendrodendritic synapses: past, present, and future. *Ann. N Y Acad. Sci.* **1170**, 215–223.
- Shepherd, G.M., Chen, W.R., Willhite, D., Migliore, M., and Greer, C.A. (2007). The olfactory granule cell: from classical enigma to central role in olfactory processing. *Brain Res. Brain Res. Rev.* **55**, 373–382.
- Shu, X., Lev-Ram, V., Deerinck, T.J., Qi, Y., Ramko, E.B., Davidson, M.W., Jin, Y., Ellisman, M.H., and Tsien, R.Y. (2011). A genetically encoded tag for correlated light and electron microscopy of intact cells, tissues, and organisms. *PLoS Biol.* **9**, e1001041.
- Siepka, S.M., and Takahashi, J.S. (2005). Methods to record circadian rhythm wheel running activity in mice. *Methods Enzymol.* **393**, 230–239.
- Sur, M., Esguerra, M., Garraghty, P.E., Kritzer, M.F., and Sherman, S.M. (1987). Morphology of physiologically identified retinogeniculate X- and Y-axons in the cat. *J. Neurophysiol.* **58**, 1–32.
- Tamamaki, N., Uhlrich, D.J., and Sherman, S.M. (1995). Morphology of physiologically identified retinal X and Y axons in the cat's thalamus and midbrain as revealed by intraaxonal injection of biocytin. *J. Comp. Neurol.* **354**, 583–607.
- Welsh, D.K., Takahashi, J.S., and Kay, S.A. (2010). Suprachiasmatic nucleus: cell autonomy and network properties. *Annu. Rev. Physiol.* **72**, 551–577.

- Williams, R.W., and Chalupa, L.M. (1983). An analysis of axon caliber within the optic nerve of the cat: evidence of size groupings and regional organization. *J. Neurosci.* 3, 1554–1564.
- Williams, S.R., and Stuart, G.J. (2002). Dependence of EPSP efficacy on synapse location in neocortical pyramidal neurons. *Science* 295, 1907–1910.
- Wong, K.Y., Dunn, F.A., Graham, D.M., and Berson, D.M. (2007). Synaptic influences on rat ganglion-cell photoreceptors. *J. Physiol.* 582, 279–296.
- Yan, L., and Silver, R. (2002). Differential induction and localization of mPer1 and mPer2 during advancing and delaying phase shifts. *Eur. J. Neurosci.* 16, 1531–1540.
- Yokoi, M., Mori, K., and Nakanishi, S. (1995). Refinement of odor molecule tuning by dendrodendritic synaptic inhibition in the olfactory bulb. *Proc. Natl. Acad. Sci. USA* 92, 3371–3375.

STAR★METHODS**KEY RESOURCES TABLE**

REAGENT or RESOURCE	SOURCE	IDENTIFIER
Antibodies		
Rabbit polyclonal anti-miniSOG	A gift from Roger Tsien's laboratory	N/A
Rabbit polyclonal anti-VIP	Immunostar	Cat# 20077; RRID: AB_572270
FluoroMyelin	Thermo Fisher Scientific	Cat# F34652; RRID: AB_2572213
Bacterial and Virus Strains		
AAV2-EF1 α -DIO-miniSOG-f	The Salk vector core	N/A
AAV2-EF1 α -DIO-tdTomato-f	The Salk vector core	N/A
Chemicals, Peptides, and Recombinant Proteins		
Normal donkey serum	Jackson ImmunoResearch	Cat# 017-000-001
Glutaraldehyde	Electron Microscopy Sciences	Cat# 16200
Paraformaldehyde	Electron Microscopy Sciences	Cat# 19200
Glycine	Electron Microscopy Sciences	Cat# 16200
Potassium cyanide	Electron Microscopy Sciences	Cat# 19200
Aminotriazole	Sigma-Aldrich	Cat# G7126
3,3'-Diaminobenzidine Free Base	Sigma-Aldrich	Cat# D8801
Potassium ferrocyanide	BAKER ANALYZED® A.C.S. Reagent	Cat# 3114
Osmium tetroxide	Electron Microscopy Sciences	Cat# 19150
Thiocarbohydrazide	Electron Microscopy Sciences	Cat# 21900
L-aspartic acid	Sigma-Aldrich	Cat# A93100
Lead nitrate	Electron Microscopy Sciences	Cat# 17900
Durcupan ACM resin, Component A/M	Sigma-Aldrich	Cat# 44611
Durcupan ACM resin, Component B	Sigma-Aldrich	Cat# 44612
Durcupan ACM resin, Component C	Sigma-Aldrich	Cat# 44613
Durcupan ACM resin, Component D	Sigma-Aldrich	Cat# 44614
Deposited Data		
SBEM datasets	This paper	Cell Image Library http://www.cellimagelibrary.org/home Accession number CIL: 50581, 50582, 50583, 50584, 50643 and 50644
Experimental Models: Organisms/Strains		
<i>Opn4</i> ^{Cre/+} mice	Hatori et al., 2008	N/A
Software and Algorithms		
ClockLab	Actimetrics	RRID:SCR_014309
IMOD	http://bio3d.colorado.edu/imod	RRID:SCR_003297
Cascaded hierarchical model (CHM)	https://github.com/slash-segmentation/CHM	N/A
Imaris	Bitplane Inc	RRID:SCR_007370

LEAD CONTACT AND MATERIALS AVAILABILITY

Further information and requests for resources and reagents should be directed to and will be fulfilled by the Lead Contact, Satchidananda Panda (Satchin@salk.edu). There are restrictions to the availability of the viruses used in this study due to material transfer agreements covering various aspects of these viruses.

EXPERIMENTAL MODEL AND SUBJECT DETAILS

Animals

All animal experiments and use were approved by the Salk Institute IACUC. Male and female *Opn4*^{Cre/+} mice between 2 and 6 months of age were used for protocol optimization, circadian wheel-running assays, and tissue collections. All mice were group housed (< 5 per cage) under standard 12 h light (~100 Lux light at cage level) and 12 h darkness, ~22°C room temperature and fed a standard laboratory chow. All tissue samples were collected between Zeitgeber time (ZT) 4 and ZT6. All SBEM data are from one male mouse. Immunostaining data are from at least three mice from both sexes.

METHOD DETAILS

Vector Construction

A farnesyl sequence was cloned into the 3' end of the miniSOG construct (Shu et al., 2011) and was inserted in an inverted orientation between the lox sites in an AAV2-DIO vector (Cardin et al., 2009) to create AAV2-DIO-miniSOG-f. AAV2-DIO-miniSOG-f and AAV2-DIO-tdTomato-f were produced by the Salk Gene Transfer, Targeting and Therapeutics Viral Vector Core Facility at titers of 1.09×10^{11} TU/ml and 9.41×10^{11} TU/ml respectively. As miniSOG has relatively less quantum yield, it is prone to rapid bleaching upon photoexcitation, thus making it difficult to select a region of interest for further analyses. To enable extended search of the ROI under a fluorescent microscope, we co-injected the miniSOG virus with tdTomato-f virus to the *Opn4*^{Cre/+} mice.

Vector Injection

The Cre-dependent genetic markers are the reliable reporters of Cre-expressing ipRGCs in *Opn4*^{Cre/+} mice (Brown et al., 2010; Hatori et al., 2008). This approach, as opposed to the transgenic expression of a reporter from the native *Opn4* promoter, reliably marks nearly all ipRGCs (Brown et al., 2010). To express miniSOG and tdTomato ipRGCs, 3 μ l of AAV2-EF1 α -DIO-miniSOG and 0.3 μ l of AAV2-EF1 α -DIO-tdTomato was injected into both eyes of *Opn4*^{Cre/+} mice between the ages of 2 and 6 months old. Anesthesia was induced and maintained with isoflurane. 0.5% proparacaine (Bausch and Lomb) is applied to each eye prior to any surgical intervention to provide topical analgesia. The mouse is placed within the field of view of the dissection microscope such that the left eye is completely visible. Curved forceps are used to place gentle pressure around the eye such that the globe of the eye is raised slightly out of the orbit and the edge of the sclera is visible. A small incision is made with a 31-gauge insulin needle 0.5 mm posterior to the limbus of the eye (the region where the sclera meets the cornea). Vector is loaded into a Hamilton microliter syringe with a 34-gauge beveled needle that is mounted on a micromanipulator. The micromanipulator is used to maneuver the loaded needle through the incision made by the insulin needle such that the tip of the needle ends up in the vitreous in the middle of the eye. Vector is slowly injected over the course of 1 minute and allowed to diffuse through the vitreous for 3 minutes before the needle is slowly withdrawn. The whole procedure is then repeated on the right side. After both eyes of been injected, GenTeal lubricant eye gel (Novartis) is applied to both eyes and the animal is removed from isoflurane anesthesia and placed in a clean cage to recover. When righting reflex is restored after 1-2 minutes, the animal is returned to its home cage.

Circadian Wheel Running

The daily locomotor activity of mice intravitreally injected with AAV2-EF1 α -DIO-miniSOG-f and AAV2-EF1 α -DIO-tdTomato, a different GFP expressing AAV2-DIO vector, and age-matched uninjected mice was measured following established methods (Siepka and Takahashi, 2005). Briefly, one month after virus injection, mice were individually housed in cages with *ad libitum* access to standard mouse chow and a running wheel connected to a counter that reported wheel rotations to a computer. All cages were kept within one ventilated and independently lit light-tight box in the vivarium. During the light phase, which began at 6 AM and ended at 6 PM PST, the mice received ~150 lux white light from a fluorescent light source. Wheel running activity, as number of rotations, was continuously collected as 5 min bins and later analyzed by ClockLab software (Actimetrics, Evanston, IL, USA). After 11 days on a strict 12:12 light:dark cycle, the lighting conditions were changed to complete darkness for 7 days before resuming the original 12:12 light:dark conditions. All routine animal husbandry care that occurred during the dark phase was performed under dim red light illumination so as not to disrupt circadian light entrainment.

Immunofluorescence and Confocal Microscopy

For immunofluorescence labeling, miniSOG and tdTomato traced 100 μ m thick brain sections and flat mount retina were blocked in 10% normal donkey serum (NDS, Jackson ImmunoResearch, West Grove, PA, USA) in PBS for 1 h at room temperature prior to incubation with the following antibody: rabbit polyclonal anti-miniSOG antibody (Gift from Roger Tsien's laboratory) and rabbit polyclonal anti-VIP (Immunostar) in 10% NDS for 16 h at 4°C. Fluorescence-conjugated secondary antibodies were applied at 1:100 dilution for 4 h at 4°C and then washed with PBS. For myelin staining, the sections were stained with FluoroMyelin (Invitrogen, Carlsbad, CA, USA). Images were acquired with confocal microscopy (Olympus FluoView1000; Olympus, Tokyo, Japan) and processed with Imaris software (Bitplane Inc.).

Tissue Preparation, Fluorescence Imaging, and Photooxidation of Mouse Retina and Brain

At least three weeks after intravitreal injection of AAV2-EF1 α -DIO-miniSOG-f and AAV2-EF1 α -DIO-tdTomato into *Opn4*^{Cre} mice, the mice were anesthetized with ketamine/xylazine and transcardially perfused with Tyrode's solution followed by 4% formaldehyde / 0.1% glutaraldehyde in 0.1M phosphate buffered saline (PBS). The retina and brain were dissected and post-fixed with 4% formaldehyde in 0.1 M PBS on ice for 2h and then the brain was cut into 100- μ m-thick slices. For miniSOG photooxidation, tdTomato expressed ipRGCs and ipRGC neurites were identified using a Leica SPE II inverted confocal microscope and the retina and brain tissue were fixed with 2.5% glutaraldehyde, 2.5 mM CaCl2 in 0.15 M Sodium Cacodylate buffer (CB) pH 7.4, and the tissue was rinsed with ice-cold CB, and blocked for 30 min with 50 mM glycine, 10 mM Potassium cyanide and 5 mM aminotriazole in CB. Freshly prepared diaminobenzidine (DAB free base, Sigma) in CB was added to the tissue, and ipRGCs and axons were illuminated with 450–490 nm light from a Xenon lamp for 20–25 min until a light brown reaction product was observed in place of the green fluorescence of MiniSOG. The tissue was then processed for SBEM. Although the method was optimized in several mice, all volumes presented in this manuscript were from one mouse.

SBEM Preparation and Imaging

Tissue was prepared for SBEM as previously described (Deerinck et al., 2010). Briefly, tissue was washed with 0.15 M CB and then placed into 2% OsO4/1.5% potassium ferrocyanide in 0.15 M CB containing 2 mM CaCl2. The slices were left for 30 min on ice and then 30 min at room temperature (RT). After thorough washing in double distilled water, the slices were placed into 0.05% thiocarbohydrazide for 30 min. The slices were again washed and then stained with 2% aqueous OsO4 for 30 min. The slices were washed and then placed into 2% aqueous uranyl acetate overnight at 4°C. The slices were washed with water at RT and then stained with 0.05% en bloc lead aspartate for 30 min at 60°C. The slices were washed with water and then dehydrated on ice in 50%, 70%, 90%, 100%, 100% ethanol solutions for 10 min at each step. The slices were then washed twice with dry acetone and then placed into 50:50 Durcupan ACM:acetone overnight. The slices were transferred to 100% Durcupan resin overnight. The slices were then flat embedded between glass slides coated with mold-release compound and left in an oven at 60°C for 72 h. SBEM data was collected with a 3View unit (Gatan Inc., Pleasanton, CA, USA) installed on a Merlin field emission SEM (Carl Zeiss Microscopy, Jena, Germany). The retina and brain volumes were collected in 2.0 to 2.4 kV accelerating voltages, with a raster size of 20,000 × 20,000 or 24,000 × 24,000 and pixel dwell time of 0.5 – 1.5 μ s. The pixel sizes were 4.0–7.3 nm, depending on the raster size and cutting thickness was 40–60 nm. Before each volume was collected, a low magnification (~500X) image was collected of the block face to confirm the anatomical location of the volume based on tissue landmarks, such as the SCN, IGL, dLGN, vLGN and OPN. Once a volume was collected, the histograms for the slices throughout the volume stack were normalized to correct for drift in image intensity during acquisition. Digital micrograph files (.dm4) were normalized using Digital Micrograph and then converted to MRC format. The stacks were converted to eight bit, mosaics were stitched, and volumes were manually or semi automatically traced for reconstruction and analysis. Stereology was performed using a custom plug-in for IMOD. Six datasets resulting from this publication will be released to the public through the Cell Image Library (CIL). The following volumes with specified resolutions were analyzed.

SBEM Dataset	Pixel Size (nm/pix)			Pixel Dimensions			Tissue Dimensions (μ m)			Tissue Volume (μ m ³)
	X	Y	Z	X	Y	Z	X	Y	Z	
ON	10.6	10.6	70	13000	13000	999	137.8	137.8	69.93	1327889.58
SCN	7.0	7.0	60	17000	17000	456	119	119	27.36	387444.96
OPN	7.0	7.0	60	17000	17000	596	119	119	35.76	506397.36
IGL	4.6	4.6	60	28000	20000	199	129.4	92.4	11.94	142717.20
vLGN	7.4	7.4	60	20000	20000	416	148	148	24.96	546723.84
dLGN	7.4	7.4	60	20000	20000	520	148	148	31.2	683404.80

Electron Tomography

For ET, 300nm thick sections of the SCN and OPN were collected from the tissue block with a diamond knife and placed on luxel grids. Following glow discharge, 15-nm diameter colloidal gold particles were deposited on each side to serve as fiducial markers. Data were generated on a FEI Titan microscope operating at 300 kV, with the micrographs were produced using a 4000 × 4000 Gatan Ultrascan CCD camera. Double tilt series of images were recorded with the sample tilting between –60° and +60° at regular increments of 0.5°, allowing to generate 3D reconstructions. Alignment of the projection micrographs and 3D iterative reconstruction were performed using the transform-based tracking, bundle adjustment, and reconstruction package (Lawrence et al., 2006; Phan et al., 2017).

Manual Segmentation**3D reconstruction of SCN and OPN neurons**

In order to maximize the amount of reconstructed neuronal processes from each neuron traced in the SCN and OPN, neurons were selected from the center of each image in IMOD (University of Colorado, Boulder). Each individual neuron of interest was traced as a

separate object by drawing contours around the plasma membrane of each selected cell as it moved through each slice of the image. Individual contours were meshed with *imodmesh* to reveal 3D reconstructions of the neurons of interest. In this way, cell bodies, axons, dendrites, and, in some cases, primary cilia, were identified and represented in the 3D model.

Grid-Based Selection Scheme

All boutons were sampled from the 100 intersection points of a 11X11 grid overlaid on the image stack. Alternating between panning down or up through the image stack, the first labeled bouton to intersect with the grid point, or the closest bouton to it was sampled. Subsequently, these boutons were backtraced to the limit of the volume to yield a segment of axon and more boutons. This allowed for a comprehensive and unbiased sampling of the tissue.

Synapse Quantification

Putative synapses were identified manually by finding areas of the axon that were swelled to diameters at least twice as large as the average diameter of axons. A swelling was deemed a putative synapse if it fulfilled at least two of the following three criteria: presence of a postsynaptic density in the directly apposed membrane, presence of at least one mitochondrion, or evidence of synaptic vesicles less than one vesicle diameter's distance from the plasma membrane. In order to count the number of synaptic boutons, each image volume was parsed into a 10×10 grid and the miniSOG⁺ boutons in every other square column were counted. The contours that make up each bouton were traced out and meshed with *imodmesh* to determine bouton volume, and the mitochondria and intrusions from the postsynaptic process into the bouton were counted.

Probability of finding a bouton with a spine

Each bouton was assessed for spines in a binary fashion 1 for present (1 or more spines), 0 for absent. This allows us to estimate the probability of finding a bouton with a spine. We estimate ($p = (X_1 + \dots + X_n)/n$) (the average). The binomial standard error was used $SE = \sqrt{(p(1-p)/n)}$ and values reported as: $p \pm SE$.

Proximal to distal synaptic density nonlinear regression

Axon volume

MiniSOG⁺ ipRGC axonal processes were identified by the dark miniSOG label and the outlines of the cross-section of miniSOG⁺ axon were traced to make contours of the axon in each slice of the image volume. Each individual axon was assigned a unique object number that consisted of all axon contours. Contours were meshed with *imodmesh* to render 3D reconstructions of each axon. The IMOD program *imodinfo* returned the volume of the object.

Axon length

A new open contour object was made for each axon and individual consecutive points of a single open contour were placed in the center of miniSOG⁺ axon cross-sections starting from the first slice in an image volume until the last slice in an image volume. If an axon branched, a new open contour was made for that axon object and another set of consecutive points laid down for the branch. This was repeated until the entire axon was represented by an open contour skeleton line created from consecutive points. *Imodinfo* returned the length of all lines in the object. Similar approach was used to reconstruct skeletal models of dendrites.

Dendrodendritic Chemical Synapse False Negative Correction

Given the relatively low frequency of these synapses and the limited length of dendrite captured by the sample cube, there is a non-zero probability that DDCS⁻ dendrites have falsely categorized both pre and postsynaptically. The probability of detecting such synapses is lowest in shorter dendritic segments and higher in long dendritic segments. We created a statistical model to predict the rate at which DDCS sites were missed by chance. 25 random points were selected on a 1000 unit domain to mimic 2.5 DDCS per 100 μm as observed. Random sampling intervals of the increasing range were assigned and the change in the number of random points detected as the sampling interval increased was plotted. A sigmoid function fits the data ($R^2 = 0.998$) and this function was used to predict the average rate of detection for normal distributions of dendritic lengths.

Selection of SCN and OPN neurons for detail analyses

To analyze ipRGC input synapses on the SCN and OPN neurons, we selected somas that were entirely contained within the imaged volume. We mapped ipRGC boutons on the first 75 μm of centrally located 18 neurons in the OPN volume and 77 neurons in the SCN volume. All 18 neurons examined in the OPN had at least one proximal ipRGC contact while 37 of 77 neurons in the SCN had no proximal contact. Due to a large number of SCN somas without an ipRGC synapse, 17 additional SCN somas were segmented and surveyed. Given the difference in neuron density in the OPN and SCN, the number of OPN neurons available for sampling were numerically less than the SCN neurons.

Independent assessment of proximal-distal preference of ipRGC axons

Another way to assess ipRGC target preference in the SCN was to analyze the allocation of the 502 contact sites from 36 randomly selected ipRGC axon arbors (projectome). Only 8 out of 502 (1.59%) the contact sites were directly on the soma, 41 (8.17%) on a proximal dendrite (within 75 μm of a soma), and the remaining 453 (90.24%) were either greater than 75 μm from a soma or contacted a dendrite with a soma outside of the volume. We assumed that a majority of the dendrites with no soma in the volume are likely to be greater than 75 μm from the soma. 143 (28.4%) of all contacts were to DDCS dendrites. Given that the average available length of projectome dendrites is 58.6 μm , our false negative correction equation predicts a detection rate of 71.5% and therefore the true allocation of ipRGC contacts to DDCS is likely to be ~40%.

Selection of SCN dendrites for DDCS analyses

Three different cohorts of dendrites were selected. (a) *Proximal dendrites*; all 286 neurons with soma partly or entirely contained within the imaged volume had a total of 398 dendrites. (b) *Projectome dendrites*; All postsynaptic sites touched by 38 randomly selected ipRGC axon arbors were traced back to obtain 298 dendrites. (c) *Random dendrites*: one hundred randomly selected dendrites from the intersection points of the 11x11 grid. Thirty-two of projectome dendrites were also contained within the proximal dendrite set, thus the combined set of “projectome + proximal” dendrites contained 660 dendrites. Forty-three out of the 100 randomly selected dendrites (i.e., 43%) were also contained in the “projectome + proximal” dendrite set. Therefore, we estimate there is $660/43 \times 100 = 1535$ total number of dendrites in the image volume. After accounting for overlap, the three sets altogether numbered 717 dendrites manually surveyed in each image section of the volume. The DDCS were selected based on the presence of presynaptic dense core vesicles as has been earlier detected in the rodent SCN (Castel et al., 1996). Out of the hundred randomly selected dendrites, 11 were either pre- or post-DDCS dendrites. Therefore, approximately 11% of all dendrites are likely to be part of a DDCS contact. Since we estimated the imaged volume contains ~ 1535 dendrites, there were likely $1535 \times 11/100 = 169$ DDCS dendrites within the volume. Out of these 169 estimated DDCSs within the volume, we identified 136 or $(136/169 \times 100 =) 80.5\%$ of all DDCSs.

Automatic Segmentation

Generation of Ground Truth Data

A $5,000 \times 5,000 \times 100$ voxel sub-volume of the full SBEM dataset was extracted to yield a set of ground truth images. All miniSOG-stained ipRGC axons contained within this set were manually segmented to provide ground truth labels, and the accuracy of these labels was verified independently by two experts. Following observation of the ground truth labels, three classes of ipRGC axons were qualitatively identified within the SBEM volume based upon the strength and variation of voxel intensity levels across image planes. In the first class of Densely Stained (DS) axons, the staining was consistently dark throughout all cross-sectional planes of the axon, resulting in low voxel intensity values and low inter-plane variances. For the second class of Sparsely Stained (SS) axons, the staining was consistently light throughout the cross-sectional planes of the axon. The final class, Variably Stained (VS) axons, exhibited staining that was inconsistent, with some regions of dense staining and some regions of sparse staining. The 96 individual axon segments contained within the ground truth labels were automatically classified into one of these three groups via k-means clustering ($k = 3$) of the mean voxel intensity of the entire axon segment and the range of the mean voxel intensities for all cross-sectional planes.

Cascaded Hierarchical Model Training

A $500 \times 500 \times 50$ set of training images and labels for the DS axon class was generated via manual segmentation. The training images consisted of tiles interspersed throughout the breadth and depth of the full SBEM volume, and decisions on whether each cross-sectional axon profile encountered belonged to the DS class were made qualitatively. The same process was then repeated to yield an equally sized set of training images and labels for the SS axon class. Unique voxel classifiers were trained for the DS and SS classes using the cascaded hierarchical model (CHM) with two stages and two levels (Seyedhosseini et al., 2013).

Semi-automatic Axon Segmentation

Each trained voxel classifier was applied to the full SBEM stack to yield two sets of probability maps, one for DS axons and one for SS axons. All probability maps were segmented by evolving 2D active contours from automatically seeded initial positions, as previously described (Perez et al., 2014). A number of post-processing steps were then performed to enhance segmentation accuracy. A final, combined segmentation stack was generated by taking the voxel-by-voxel logical disjunction of the DS and SS segmentation stacks and running a hole filling operation on the output. Three-dimensionally connected components were computed across the entire segmentation volume using the IMOD (Kremer et al., 1996) programs *imodauto* and *imodsortsurf*. The output connected components were then morphologically filtered using the Pylmod set of Python modules for manipulating IMOD binary model files (<https://github.com/CRBS/PylMOD>). Two rounds of filtering were performed; first, components with any cross-sectional area greater than $6 \mu\text{m}^2$ were removed to reduce the occurrence of common false positives such as non-labeled myelin sheaths and regions of charging within cell nuclei and blood vessels. Second, components that did not persist across the depth of the stack for greater than $2 \mu\text{m}$ were removed to reduce the prevalence of common false positives such as densely stained lysosomes. Surface renderings of the filtered results were produced using *imodmesh*, converted to the VRML format, and displayed in Amira (FEI Company, Hillsboro, OR). Segmentation quality was assessed by comparison of the final results to the manually generated ground truth labels over the $5,000 \times 5,000 \times 100$ voxel ground truth sub-volume. Precision or the Positive Predictive Value is true positive (TP)/[TP+False Positive (FP)]. Recall or Sensitivity is the proportion of Real Positive (ground truth) cases that are correctly Predicted Positive. F-value is $(2 \times \text{TP})/(2 \times \text{TP} + \text{FP} + \text{FN})$, where FN is false negative (Powers, 2011). The semi-automated segmentation workflow yielded an F-value of 0.66537 over the region of ground truth tested. By comparison, the same workflow applied to only the results from the DS axon segmentation produced an F-value of 0.51479. Therefore, as expected, the process of training separate DS and SS axon models and combining their results via logical disjunction dramatically improved final segmentation quality. Seventy-eight percent of the axon segments within the ground truth volume that persisted for more than a few sections were at least partially annotated in the final segmentation.

QUANTIFICATION AND STATISTICAL ANALYSIS

Data are presented as the mean \pm standard error of the mean. Differences between different regions of SBEM were analyzed with GraphPad Prism software and the statistical methods used for comparison between pairs, among groups of brain regions or curve fit are indicated in Table S1 and under respective figure legends. In summary datasets with more than two groups were analyzed with one-way ANOVA and Bonferroni corrected for multiple comparisons. Datasets with two group were analyzed with a Student's t test. Significance was taken as $p < 0.05$.

DATA AND CODE AVAILABILITY

The raw SBEM volumes generated during this study are available at the Cell Image Library (<http://www.cellimagelibrary.org>) under accession number CIL: 50581, 50582, 50583, 50584, 50643 and 50644. The CHM source code and documentation are freely available at the following GitHub URL: <https://github.com/slash-segmentation/CHM>. Additional supporting data of this study are available within the supplementary information files.